



DISSERTATIONES ASTRONOMIAE UNIVERSITATIS TARTUENSIS

11

**STRUCTURE  
OF DISTANT DISK GALAXIES**

**ANTTI TAMM**



TARTU UNIVERSITY  
PRESS

The study was carried out at the Institute of Theoretical Physics, University of Tartu, Estonia.

The dissertation was admitted on March 8, 2006, in partial fulfilment of the requirements for the degree of Doctor of Philosophy in physics (astrophysics), and allowed for defense by the Council of the Department of Physics, University of Tartu.

Supervisor: Dr. Peeter Tenjes, Institute of Theoretical Physics,  
University of Tartu, Estonia

Opponents: Dr. Nils Bergvall, Uppsala Astronomical Observatory, Sweden  
Dr. Jaan Vennik, Tartu Observatory, Estonia

Defense: April 20, 2006, at the University of Tartu, Estonia

ISSN 1406–0302  
ISBN 9949–11–288–5 (trükis)  
ISBN 9949–11–289–3 (PDF)

Autoriõigus Antti Tamm, 2006

Tartu Ülikooli Kirjastus  
[www.tyk.ee](http://www.tyk.ee)  
Tellimus nr. 182

# Contents

<b>List of original publications</b>	<b>7</b>
<b>1 Introduction</b>	<b>8</b>
<b>2 Overview</b>	<b>10</b>
2.1 General cosmological framework . . . . .	10
2.2 Galaxy formation scenarios . . . . .	12
2.3 Observations of general evolution . . . . .	14
2.4 Evolution of the properties of disk galaxies. Motivations for the present work . . . . .	17
<b>3 Methodology</b>	<b>20</b>
3.1 Requirements for observations . . . . .	20
3.2 The sample . . . . .	21
3.3 Processing the original observations . . . . .	25
3.3.1 Image reduction . . . . .	25
3.3.2 PSF deconvolution . . . . .	26
3.3.3 Isophote fitting . . . . .	27
3.3.4 Photometric calibrations . . . . .	28
3.3.5 Recalibrating the rotation curves . . . . .	30
3.4 Modeling . . . . .	31
3.4.1 Sérsic approximation for luminosity distribution . .	31
3.4.2 Luminosity distribution from space density distribution	34
3.4.3 Self-consistent mass distribution modeling . . . . .	35
3.4.4 Dark matter distribution . . . . .	36
3.4.5 Model fitting. Limitations of the final models. . . . .	38
<b>4 Results and discussion</b>	<b>42</b>
4.1 Luminosity profiles . . . . .	42
4.2 Disk sizes . . . . .	44

4.3	$(U - V)$ colors . . . . .	46
4.4	Color gradients . . . . .	47
4.5	Masses and mass-to-light ratios . . . . .	48
4.6	Uncertainties of the study . . . . .	50
<b>5</b>	<b>Conclusions</b>	<b>53</b>
	<b>References</b>	<b>54</b>
	<b>Kokkuvõte</b>	<b>62</b>
	<b>Acknowledgements</b>	<b>64</b>
	<b>Publications</b>	<b>65</b>

# List of original publications

The thesis consists of a review of the three original papers listed below. The papers are referred by the corresponding Roman numerals throughout the text.

- I A. Tamm and P. Tenjes, “*Structure and Mass Distribution of Spiral Galaxies at Intermediate Redshifts*”, 2003, *Astron. & Astrophys.*, 403, 529
- II A. Tamm and P. Tenjes, “*Structure of Visible and Dark Matter Components in Spiral Galaxies at Redshifts  $z = 0.5 - 0.9$* ”, 2005, *Astron. & Astrophys.*, 433, 31
- III A. Tamm and P. Tenjes, “*Surface Photometry and Structure of High Redshift Disk Galaxies in the HDF-S NICMOS Field*”, 2006, *Astron. & Astrophys.*, 449, 67

## Other related papers:

Tamm, A., Tenjes, P., “*Surface Photometry of Spiral Galaxies at Redshifts 0.15 to 1*”, 2001, *Balt.Astron.*, 10, 599

## Related conference presentations:

Conference “*Baryons in Dark Matter Halos*”, Oct. 5. – 9., 2004, Novigrad, Croatia. A. Tamm: “*Structure of visible and dark matter components of spiral galaxies at  $z = 0.9$* ”

Workshop “*Outer Edges of Disk Galaxies: a Truncated Perspective*”, Oct. 4. – 8., Lorentz Center, Leiden, the Netherlands. A. Tamm: “*Structure of disk galaxies out to  $z = 3$* ”

# Chapter 1

## Introduction

Why is the Space inhabited by exactly such objects as it is? Why are these object arranged into precisely such structures? What can we learn from this about the fundamental physics and the history of everything? These are the principal questions that all modern astronomers and cosmologists should be looking answers for; the rest is public relations and risk-analysis. Throughout the centuries-long history of scientific astronomy, merely the current stage of the Universe has been within the reach of researchers; multitude of hypotheses and theories, attempting to explain the origin of the stars, nebulae and other cosmic structures was to remain just a speculation, without any chance of observational confirmation; studies of the unrecorded past have been a subject for the archeologists only - until now.

During the last dozen years, the situation has changed utterly and conclusively. Observational cosmology, unimaginable just a pair of decades ago, is now a hot topic for numerous research groups all over the world. Thanks to the rapid development of observational technologies, the zoo of various structures in the Universe can be traced down almost to its very beginning. The unprecedented spatial resolution, achieved with space-based optical, ultraviolet and near-infrared imaging of cosmic objects can be supplemented with observations in the full wavelength-range of electromagnetic radiation, while a new generation of large ground-based telescopes enables to carry out spectral measurements of extremely faint distant galaxies and quasars. Extensive surveys are being carried out, detecting parameters of hundreds and thousands of distant galaxies and providing important information about the overall trends in the Universe and galactic evolution. On

the basis of these data, the powerful computational techniques of hydrodynamic simulations and semi-analytic modeling are capable of replaying and reproducing many of the complex processes, responsible for the structure formation and evolution in our Universe.

In contrast to the relative success achieved by studies of the overall properties of the early Universe, it still requires a considerable effort to conduct investigations of intrinsic properties of distant galaxies and thus a number of decisive aspects about galactic evolution is yet to be clarified observationally. In the present situation of high-quality observational data piling up in web-archives, a substantial part of such research can be done using the information already acquired with the world's top telescopes. The present thesis serves as a test for such a possibility.

The thesis concentrates on the intrinsic structure of distant disk galaxies. Radial distribution of luminosity, color and mass of a sample of galaxies is derived, in an attempt to detect possible traces of evolutionary effects on disk structure. The study is based on spatially resolved kinematics, found in the literature, and the yet unmatched imaging by the Hubble Space Telescope, retrieved from the telescope's web-archive.

The thesis can be outlined as follows. In Chapter 2, the very basic cosmological framework is described, followed by a review of the current recipes for building galaxies and the observational pieces of evidence of galactic evolution gathered so far. Chapter 3 gives an insight to the observations, data reduction and modeling methods used to reach the results described in Chapter 4 and summarized in Chapter 5.



# Chapter 2

## Overview

### 2.1 General cosmological framework

General understanding of our Universe is that of a hot big bang universe. A key property of such a universe is its global expansion, observationally discovered by Edwin Hubble already in 1920s, stating that at larger scales, all the objects are generally flying away from each other. The global expansion is described by the Friedman equation

$$H^2 \equiv \left(\frac{\dot{a}}{a}\right)^2 = \frac{8\pi G\rho_{tot}}{3} - \frac{1}{R^2}, \quad (2.1)$$

where  $H$  is the expansion rate (the Hubble parameter),  $a(t)$  is the cosmic scale factor,  $\rho_{tot}$  is the total mass-energy density (including the cosmological constant  $\Lambda$ ) and  $R \equiv k/a^2$  is the curvature radius. The curvature parameter  $k > 0$  sets a high-density, positively curved universe, while  $k < 0$  is valid for a negatively curved low-density universe. Thus the total mass-energy and spatial curvature  $k$  are linked. Defining  $\Omega \equiv \rho_{tot}/\rho_{crit}$ , where  $\rho_{crit} \equiv 3H^2/8\pi G$  is the critical density, corresponding to a flat universe with curvature  $k = 0$ , we can rewrite Eq. 2.1 as follows:

$$R = \frac{H^{-1}}{|\Omega - 1|^{1/2}}, \quad (2.2)$$

The WMAP-satellite measurements of the cosmic microwave background indicate that the geometry of our Universe is very close to being flat:  $\Omega_0 = 1.00 \pm 0.03$ , with “0” denoting the present value (de Bernardis et al. 2002).  $\Omega_0$  is currently considered to primarily consist of the share of the cosmological constant  $\Omega_\Lambda \approx 0.7$  and the share of matter  $\Omega_M \approx 0.3$ , so

that  $\Omega_0 = \Omega_M + \Omega_\Lambda$ .  $\Omega_M$  in turn seems to be dominated by cold dark matter (CDM) - particles of a yet unknown nature, not discovered to radiate at any wavelength nor seen in high-energy particle-experiments as yet, but needed to keep the motions of galaxies in concordance with the Newton's gravitational law. A flat universe with a cosmological constant is often referred to as a  $\Lambda$ CDM-cosmology.

The expansion of the Universe is responsible for the cosmological redshift  $z$ , relating the observed wavelength of a photon  $\lambda_R$  received at a time  $t_R$  to its rest-wavelength  $\lambda_E$  when emitted at time  $t_E$ ; it is also related to the change in cosmic scale factor  $a(t)$ :  $1 + z \equiv \lambda_R/\lambda_E = a(t_R)/a(t_E)$ , and thus provides a model-independent measure for look-back time.

The  $\Lambda$ CDM-cosmology is at present the most favorable framework for theoretical studies, simulations and interpretations of observations; it can successfully explain the formation of structure in the Universe from the largest cosmological scales down to galaxy clusters and single galaxies (as reviewed by Freedman & Turner 2003). Within  $\Lambda$ CDM-cosmology, structure formation is a result of a sequence of events, the current vision of which will be briefly described in the following.

Small fluctuations that were imprinted in the primordial density field are amplified by gravity, eventually leading to nonlinear collapse and the formation of dark matter (DM) halos. Global expansion and consequent cooling of the Universe causes the decoupling of matter and radiation, allowing gas to fall into the potential wells provided by the hierarchically growing DM halos, where it is shock-heated and thereafter cooled radiatively, enabling a fraction of gas to collapse to such high densities that star formation can ensue.

First stars, referred to as Population III stars, are born from the primordial dust-free, zero-metallicity gas, falling into DM minihalos with masses of the order of  $10^6 M_\odot/\text{pc}^3$ , and have to be very massive (Brom & Larson 2004). This initial stellar generation is most likely responsible for the re-ionization of the neutral hydrogen in the Universe at redshift  $z \geq 15$  (corresponding to less than 300 million years after the Big Bag), leaving a specific polarization signature in the Cosmic Microwave Background, as has been observed by the WMAP experiment (Kogut et al. 2003). Population III stars steadily enrich the environment with heavier elements than helium; at some critical point, requirements for a fundamental transition of star formation are fulfilled, allowing the birth of "normal" stars instead of the Population III (Schneider et al. 2003). The exact moment of galaxy formation to be turned on is not clear as yet, nor is clear the actual impact

of the Population III on this process. Recent observational developments concerning the Cosmic Infrared Background could perhaps fill in some gaps in this puzzle (Kashlinsky 2005, Kashlinsky et al. 2005).

Further structure formation is believed to have taken place via hierarchical clustering, with massive galaxies observed in the “local Universe” having formed through a continuous assembly of smaller units (Blumenthal et al. 1984). Large-scale matter distribution in the Universe in the form of extensive filaments and dense clumps and voids in between them, well exposed by projects like the Two-degree Galaxy Redshift Survey (Colless et al. 2001) and the Sloan Digital Sky Survey (York et al. 2000, Doroshkevich et al. 2004), is a result of similar accumulation at global extent (Melott et al. 1983, Gramann 1988).

Throughout the present work, a cosmology with the Hubble constant  $H_0 = 65 \text{ km s}^{-1} \text{ Mpc}^{-1}$  and a flat space-time ( $\Omega_0 = 1$ ) has been assumed in the calculations.

## 2.2 Galaxy formation scenarios

A successful scenario for cosmic structure formation can be recognized by its ability to create both of the two dominant galactic types observed in the local Universe: a) the featureless, roughly spherical elliptical galaxies with an  $r^{1/4}$  radial surface density distribution, gravitational force being counter-balanced by the pressure of intrinsic random motions; b) the more flattened multi-component disk galaxies with a roughly exponential density distribution, often supplemented by a characteristic spiral pattern and supported against gravity by its rotation.

The hierarchical clustering scenario is particularly successful in explaining the formation of elliptical galaxies. In his early work, Toomre (1977) proposed a collision of a pair of equal mass galaxies (so called major-merger) to be the production mechanism of an elliptical galaxy, as a result of violent relaxation (Lynden-Bell 1967) involved in merger processes. The development of pressure supported galaxies with an  $r^{1/4}$  radial surface density distribution as major-merger remnants has been confirmed observationally (e.g. Schweizer 1982, Stanford & Bushouse 1991, Hibbard & Mihos 1995, Chitre & Jog 2002) as well as reproduced in numerous numerical simulations (e.g. Barnes 1988, Hernquist 1992, Heyl et al. 1996, Bendo & Barnes 2000, Naab & Burkert 2003, Bournaud et al. 2005). Peculiar characteristics of some of the elliptical galaxies, like shells, ripples, kinematically distinct cores etc. would be difficult to explain unless merger origin is considered

(Thomson & Wright 1990, Schweizer 1998, Turnbull et al. 1999, Wilkinson et al. 2000).

Also another, fundamentally different scenario for the formation of elliptical galaxies exists, proposing the birth of galaxies at high redshifts ( $z > 5$ ) via a monolithic collapse of a gas cloud, inducing a rapid burst of star formation, followed by a quiet evolution all the way to the present era (Eggen et al. 1962, Partridge & Peebles 1967, Larson 1975, Chiosi & Carraro 2002). Such a scenario looks especially appealing in the light of discoveries of massive ellipticals at considerably high redshifts (Cimatti et al. 2004, Glazebrook et al. 2004). However, sub-millimeter surveys of high-redshift radio galaxies indicate that star formation rate may be high enough to build a massive galaxy in less than 1 Gyr (Archibald et al. 2001, Reuland et al. 2003, Stevens et al. 2003 etc), helping to reconcile early ellipticals also with the hierarchical mass accumulation paradigm.

The origin of the more complex disk galaxies is somewhat less clear. Their spheroidal component is probably formed similarly to elliptical galaxies or by secular evolution (as reviewed by Kormendy & Kennicutt 2004). Theoretically, a disk can be formed if gas retains most of its angular momentum, once gained by torques from nearby structures while cooling inside a DM halo (White & Rees 1978, Fall & Efstathiou 1980, Fall et al. 1998). Simulating the formation processes of disks becomes difficult however, as a realistic model has to consider a number of sophisticated sub-processes. The early numerical works accounting for radiative cooling by hydrogen and helium, star formation and feedback processes and models of chemical enrichment achieved limited success in creating rotationally supported disks, but basically failed to reproduce the observable properties of their counterparts (Katz & Gunn 1991, Navarro & Benz 1991, Navarro & White 1993, Steinmetz & Müller 1994). Mainly, the simulated disks were too small and too centrally concentrated if compared to actual galaxies - dynamical friction suffered by dense gas lumps caused dramatic angular momentum loss (Navarro & White 1994). In addition, star formation efficiency was too high, resulting in a too large fraction of gas being converted into stars by the present epoch.

More recent simulations have given somewhat more promising results. Implementation of photoheating of gas by the UV background, using the observational Tully-Fisher relation for constraining the hierarchical clustering, accounting for multiple phases of gas as well as applying elaborate constraints on cooling and feedback mechanisms have enabled to create disks with significantly more realistic properties than initially (Navarro &

Steinmetz 2000, Sommer-Larsen et al. 2003, Abadi et al. 2003a&b, Samland & Gerhard 2003, Governato et al. 2004, Robertson et al. 2004). However, these simulations still involve a number of free parameters, usually inserted “by hand” in order to get the results concordant with observations, without an actual physical background behind their values (Cole et al. 2000). To reduce the contribution of such shepherding presumptions, more observational data have to be acquired.

## 2.3 Observations of general evolution

Tracking and studying high-redshift galaxies living in the young Universe is a challenging but essential task, necessary for setting constraints on the whole cosmological framework as well as on the simulations of individual objects. The nature and properties of high redshift galaxies are mainly investigated by measuring relatively easily detectable quantities for large samples of galaxies. These quantities include luminosity, colors, sizes and the relative abundance of different morphological types; with some assumptions applied, also star formation rates and approximate stellar masses can be deduced. Provided a considerable range of redshifts is involved and the samples are large enough for being statistically reliable, effects of evolution can be found.

*General morphology.* Despite the inevitable presence of selection effects, several important conclusions have been reached in studies of overall morphology. Hierarchical evolution predicts that, with an increasing redshift, the relative number of elliptical galaxies should diminish with respect to disks and irregulars. Indeed, number counts of galaxies in deep surveys confirm this picture. Besides, beyond  $z \approx 0.5$ , a substantial population of galaxies does not fit into the Hubble classification scheme at all; at redshifts higher than  $z \approx 1$ , these galaxies become dominant (Glazebrook et al. 1995, van den Bergh et al. 2001, Cassata et al. 2005). Such developments can be reconciled with a higher merging fraction at earlier epochs, responsible for distorting galactic outlooks as well as causing irregular shapes of young, non-virialized galaxies. On the other hand, the relative lack of elliptical galaxies, witnessed at  $z > 1.5$  (Franceschini et al. 1998, Barger et al. 1999), also supports the hierarchical galaxy formation model, which predicts that ellipticals generally form through mergers of disk galaxies at moderate redshifts (Kauffmann & Charlot 1998).

*Luminosity function.* Any simulation attempting to reproduce the evolution of galaxies has to consider the luminosity function (LF) - the relative

number of galaxies of a given luminosity. The LF of field galaxies at a given epoch depends on the star formation history in each galaxy and gravitational growth of structures via merging. Therefore, a comparison of the LF at different look-back times is a useful diagnostics tool for the physical processes acting in the formation and evolution of galaxies. To determine the LF, large and deep redshift surveys are carried out. Since the energy output at different wavelengths is dominated by stars of different mass, multi-color imaging proves beneficial. The local LF is well constrained by the results of surveys like the Two-Degree Field Redshift Survey (Norberg et al. 2002), the Two-Micron All Sky Survey (Jarrett et al. 2000) and the Sloan Digital Sky Survey (Blanton et al. 2003). Comparison with high redshift LFs (Lilly et al. 1995, Lin et al. 1999, Steidel et al. 1999, de Lapparent et al. 2003, Wolf et al. 2003, Gabasch et al. 2004, Ilber et al. 2005 etc) shows several signs of evolution. The co-moving density of bright galaxies increases with redshift; the effect is stronger for bluer galaxies, referring to an increasing rate of global star formation. Semi-analytic models (e.g. Kauffmann et al. 1999, Menci et al. 2002) still struggle to explain the observed luminosity function: star formation is too efficient, resulting in an excess of very luminous galaxies (Benson et al. 2003). Also, discrepancies increase with increasing redshift (Gabasch et al. 2004).

*Colors.* Another means for detecting evolutionary imprints is looking at color distribution of galaxies at different redshifts. In the first order, a color bi-modality is seen over the whole redshift range explored so far, distinguishing a bluer population of star-forming disk galaxies from redder early-type galaxies. For the blue population, colors show reddening since  $z \approx 1$ , while the number of luminous galaxies has decreased (Bell et al. 2004). A tendency of brighter early-type galaxies to be redder in colors, valid for both cluster and field galaxies and known as the color-magnitude relation (e.g. Visvanathan & Sandage 1977, Dressler 1980, Kodama & Arimoto 1997, Bernardi et al. 2003) is of particular interest: the relation is interpreted as a metallicity sequence, in which massive galaxies are also more metal-rich. Colors have evolved in a way that is consistent with quiescent aging of an ancient stellar population (van Dokkum et al. 2000, Blakeslee et al. 2003). Such studies require very large samples, as the change of colors depends both on galactic brightness and environment (Tanaka et al. 2005).

*Star formation rate.* By studying optical spectra and colors of galaxies, star formation rate at different look-back times can be estimated. Observations of young stars in galaxies at different redshifts indicate that some

5 – 8 billion years ago (corresponding to redshift  $0.5 < z < 1$ ), the global star formation rate was at its maximum, followed by a gradual decline until the present time (Gallego et al. 1995, Lilly et al. 1996, Connolly et al. 1997, Cowie et al. 1999, Ouchi et al. 2004, Heavens et al. 2004); such developments match well with the general reddening of disk galaxies mentioned above. However, in contrast to this global star formation, the epoch of maximal star formation of a given galaxy is a function of its total stellar mass. For example, the most massive galaxies have experienced a major peak at  $z = 2 - 3$  (Heavens et al. 2004).

*Fundamental Plane.* Stellar population history in elliptical galaxies can also be investigated by analyzing a set of well-correlated, directly observable parameters of luminosity, central velocity dispersion and surface brightness, together forming the Fundamental Plane (FP; Faber & Jackson 1976, Dressler et al. 1987, Djorgovski & Davis 1987). The slope of the FP constrains systematic age trends with mass and other parameters. Any evolution of the slope of the FP with redshift implies that ages of the stellar populations are related to galaxy mass; in an attempt to detect these effects, the high-redshift FP is being studied actively (Kelson et al. 1997, van Dokkum et al. 2001, Treu et al. 2001, Wuyts et al. 2004, Holden et al. 2005). The slope of the correlations basically remains unchanged to  $z \approx 1$ , but a decrease of the mass-to light ratio has been established – the luminosity drops as the time goes on. The studied galaxies suit into the picture of passive evolution, with the last epoch of major star formation around  $z \approx 2 - 3$ .

*Lyman-break galaxies.* The rapid development of telescopes enables to look at galaxies at higher and higher redshifts. On the other hand, spectroscopic identification of distant galaxies is time-consuming and cannot produce large samples. A powerful technique for determining galaxies at high redshifts is the Lyman-break method, exploiting deep, dominantly ground-based observations through filter passbands close to the redshifted 91.2 nm Lyman limit (Steidel & Hamilton 1992). Galaxies identified this way, the Lyman-break galaxies (LBGs), are under extensive inspection and provide large samples of high-redshift galaxies, allowing considerable statistics (e.g. Adelberger et al. 1998, Sawicki & Yee 1998, Papovich et al. 2001, Allen et al. 2005, Ivison et al. 2005). Studies indicate that LBGs are actively forming stars, contributing a significant fraction to the star formation at  $z = 2.5 - 5$  (Adelberger & Steidel 2000). They show a modest dust attenuation and are most likely progenitors of early-type galaxies, embedded in massive dark matter halos (Papovich et al. 2001, Shapley et al.

2001). LBGs can be used as tracers of very early clustering and thus enable a straightforward test of cosmological models (Miley et al. 2004, Allen et al. 2005, Ouchi et al. 2005). The Lyman break method is also being used for detecting extremely high-redshift galaxies; by now, several galaxies already at  $z \approx 10$  have been discovered (Bouwens et al. 2004, 2005). These very young galaxies are remarkably compact and produce a considerable UV-flux. What is not clearly established yet is the actual fraction which the LBGs form among all galaxies at high redshifts, thus the usage of LBGs as representatives of young galaxies in general is somewhat questionable, until possible selection effects can properly be accounted for.

## 2.4 Evolution of the properties of disk galaxies. Motivations for the present work

Studying disk galaxies at high redshifts requires a painstaking effort, as the cosmological dimming by the factor of  $(1+z)^4$  efficiently dilutes the light from the extended disks into the background noise. Getting a picture of their kinematics is even more problematic, because instead of measuring velocity dispersions, spatially resolved rotation curves have to be constructed, for which the faint light from each narrow region along a galactic image has to be spread over a range of detector pixels. Owing to these aspects, not much is known about the evolution of even the most principal intrinsic properties of distant disks. However, such knowledge is essential for constructing and constraining disk formation scenarios.

*Surface brightness.* Surveys indicate that, in addition to general reddening, disks seem to have undergone a devolution in surface brightness since  $z = 1$  (Schade et al. 1996, Roche et al. 1998, Simard et al. 1999, Böhm et al. 2004), which can be explained with a star formation decrease as a result of gas depletion.

*Disk size.* Both theory and models also suggest a certain size evolution, owing to an angular momentum scaling with the dark halo mass (Fall & Efstathiou 1980, Bouwens & Silk 2002). Dependently on model details, different radius scaling with redshift has been proposed, thus an observational determination of such a trend would have significant importance. Despite the seemingly easy task, observations have given somewhat discrepant results. While in several papers, disk size evolution has been detected at least since  $z \approx 3$  and its scaling with redshift has been estimated (Ferguson et al. 2004, Trujillo et al. 2004, 2005), some authors claim that such trends may be a mere effect of selection (Ravindranath et al. 2004, Cassata et al



2005). The situation is further worsened by the tendency of galactic outlook to change with the rest-frame imaging wavelength used for imaging (e.g. Windhorst et al. 2002, Papovich et al. 2003).

*Tully-fisher relation.* Not much knowledge has been acquired by measurements of disk kinematics. Similarly to elliptical galaxies, a remarkable correlation between fundamental parameters also exists for disk galaxies – absolute luminosity  $L$  and maximum rotation velocity  $V_{max}$  obey the Tully-Fisher relation  $L \sim V_{max}$  (Tully & Fisher 1977). By now, maximum rotation velocities have been measured and the corresponding Tully-Fisher diagrams constructed for galaxies at redshifts up to  $z = 1.2$  (Ziegler et al. 2003, Conselice et al. 2005a). No significant evolution with redshift has been witnessed. Using kinematically estimated mass, Böhm et al. (2004) have detected brightening of galaxies with respect to mass at higher redshifts, referring to a mass-to-light ratio evolution similar to that of elliptical galaxies.

*Radial distribution of disk parameters.* Very little is known about detailed radial distribution of brightness, colors and velocities of distant disks. Rotation curves for disk galaxies at up to  $z \approx 1$  have been measured by Vogt et al. (1996, 1997) and Böhm et al. (2004) and some success has been achieved in measuring the rotation of galaxies even at  $z > 2$  (Erb et al. 2003). Moth & Elston (2002) have studied Hubble Deep Field North and constructed rest-frame ( $UV_{218} - U_{300}$ ) color profiles and rest-frame  $B$  surface brightness profiles for 83 galaxies at  $z = 0.5 - 3.5$ . They report of color gradient  $\Delta(UV_{218} - U_{300})/\Delta r$  rising with redshift; the detected blueing of the central parts of galaxies at high redshifts suggests a more concentrated star formation. Recently, outer disk behavior has been studied by Pérez (2004) and Trujillo & Pohlen (2005) up to  $z \approx 1$ . These studies indicate that the position of disk truncation (the “break-point” appearing in some disk surface brightness profiles) has shifted outward with time – possibly a consequence of inside-out growth sequence of disks.

As one can see, the general picture is missing detailed data near  $z = 1$  and beyond. The available intrinsic kinematical information has not been treated consistently with the corresponding luminosity distribution, thus neither luminous nor dark matter distribution has been estimated. At higher redshifts, the interesting detection of an evolution of radial color distribution by Moth & Elston (2002) are lacking of a clear segregation of different morphological types. A dominant reason for these shortcomings lies in the finite capability of the available observational equipment. For studying individual high-redshift galaxies in detail, extremely time-consuming

observational programs on the best telescopes have to be conducted for acquiring both spectral and photometric data. Therefore, shallower studies are preferred, providing larger samples, and less attention is paid to more elaborate research. However, while the amount of observational data is piling up rapidly, it is not always necessary to take ones own exposures of distant objects; a lot of work can be done using solely the shots already taken.

The present study is an attempt to take a look at the internal properties of disk galaxies at the highest redshifts reachable at present, taking an advantage of deep observations already conducted with the best telescopes – imaging by the Hubble Space Telescope and spectra acquired with the Keck telescope and the ESO’s Very Large Telescope. The aim is to study intrinsic photometric properties of disks by constructing self-consistent mass-distribution models. The redshift range of such work is limited by spectral observations; with the supplements and restraints by kinematical information abandoned, also a solely photometric study is conducted, for which the redshift range and thus also the look-back time can be extended significantly further.

# Chapter 3

## Methodology

### 3.1 Requirements for observations

For a structural analysis, observations of high redshift galaxies need to match several severe criteria. Due to small angular sizes of galaxies at high redshifts (usually 1 – 3 arcseconds at a redshift range  $z = 0.5 - 3$ ), high-resolution imaging is necessary, with the projected angular size of pixels 0.1 arcseconds or less. This means that even with the help of adaptive optics, ground-based imaging is not good enough for detailed photometry of distant galaxies; as of now, only the Hubble Space Telescope (HST) can offer the required resolution so far; the statement is valid for optical as well as near-infrared wavelengths. The resolution of space-based observations is mainly limited by diffraction from the aperture; thus the actual physical resolution of the cameras can be raised with the application of dithering - taking exposures of the same field, shifted by just a fraction of the angular size of a pixel. The usage of dithering in deep surveys like the Hubble Deep Field North (HDF-N) and South (HDF-S) and the Ultra Deep Field (UDF) makes these and analogous forthcoming projects indispensable for studies of the high-redshift Universe.

With increasing redshift, the cosmological dimming by a factor of  $(1 + z)^4$  effectively decreases the surface brightness of galaxies; thus extremely deep imaging, with detectable surface brightness lower than  $\mu \approx 25$  magnitudes per square arcsecond is essential. To reach these depths with the HST, the total exposure time has to be at least several hours. Once again, the deep surveys mentioned above turn out to be most suitable in this aspect.

For the photometrical measurements of galaxies at different redshifts to

be comparable, the rest-wavelength of galactic imaging should be approximately uniform over the whole redshift range. Galactic morphology tends to depend on the wavelength of the observations; the effect is strongest for S0-Sb Hubble types (Papovich et al. 2003). Therefore, multiple wave-band observations are necessary.

If rest-frame optical photometry is desired, near-infrared (NIR) observations are required for galaxies at  $z > 1$ . The only camera at present, providing NIR imaging in multiple wavebands with the required resolution is the Near Infrared Camera and Multi-Object Spectrometer (NICMOS) aboard the HST. Among the three NICMOS cameras, NIC-3 is the preferred choice for larger surveys; although with lower resolution, it provides a significantly wider field of view than NIC-1 and NIC-2. At intermediate redshifts, also  $I_{815}$  filter observations of Hubble’s WFPC2 camera and  $I_{815}$  and  $z_{850}$  filter observations of the ACS can be used.

If mass distribution modeling is to be conducted, rotation curves (RCs) derived from high spatial resolution spectroscopy will be required. For this purpose, only very large ground-based telescopes (10-meter Keck telescopes and ESOs 8-meter VLT) are capable of collecting enough signal in reasonable time. Even in the best case, RCs with sufficient radial extent of galaxies at up to  $z \approx 1$  can be derived. Moreover, only galaxies with regular kinematics (i.e. with symmetric RCs) can be used for derivation of radially averaged mass distribution. Thus just a fraction of the measured RCs can actually be used for modeling.

## 3.2 The sample

Not many RCs of distant galaxies have been measured so far; fewer still qualify for mass modeling. Vogt et al. (1996, 1997) have used the Keck telescope to measure rotation curves of 16 disks at  $0.14 < z < 1$ . We chose 6 of these for studying mass distribution; the rest had either too limited spatial extent ( $V_{rot}$  did not reach the “plateau”) or were too asymmetric. Rigopoulou et al. (2002) have measured RCs of four disks at  $z \approx 0.5$  with the ESO’s Very Large Telescope (VLT). Out of these, one galaxy matched the necessary criteria. A number of RCs for disks at  $z > 2$  have been constructed by Erb et al. (2003), but these lack of spatial extent as well as deep HST images. More recently, Böhm et al. (2004) have conducted a more extensive survey and measured kinematics of 113 disks at  $0.1 < z < 1.0$  in the FORS Deep Field with the VLT; also the HST imaging has been acquired. From the published 18 RCs, some could serve

our analysis as well; the authors have not made the digital data available yet though.

Our mass distribution analysis is currently based on the 7 disk galaxies from the paper by Vogt et al. (1996) and Rigopoulou et al. (2002), with spectroscopically determined redshifts in the range  $0.15 < z < 1$ . For photometry, observations with the HST's WFPC2 camera  $V_{606}$  and  $I_{814}$  filters are available, acquired within the campaigns of the Groth Survey Strip (GSS, Koo et al. 1996), the Medium Deep Survey (MDS, Griffiths et al. 1994, Forbes et al. 1994) and the Hubble Deep Field South (HDF-S, Williams et al. 2000). General information about these observations is presented in Table 1. We retrieved these observations from the web-archive of the Space Telescope Science Institute; images of the 7 galaxies can be found in papers I and II. Considering the redshifts of the galaxies, the available observations allow the derivation of rest-frame  $B$  photometry, after the application of reasonably low  $k$ -corrections (see Sect. 3.3.4).

For a purely photometric analysis, the sample can be extended to significantly higher redshifts. We use the high-resolution near-infrared imaging of the NICMOS camera for this purpose. Several projects have exploited the NICMOS camera aboard the HST for surveys; in addition, the NICMOS has gathered exposures of countless random fields in the sky in parallel with pointed observations by the other HST instruments (Corbin et al. 2000). Unfortunately, the depth of these observations usually remains too low for detecting ordinary galaxies at  $z > 1$ ; NICMOS observations with exposure time comparable to that of the deepest HST surveys have to be used. At present, a deep enough look has been taken only at four fields in the sky with the NICMOS: the HDF-N (Thompson et al. 1999), the UDF (Thompson et al. 2005) and the NICMOS parallel fields of the HDF-S and UDF. For the UDF fields, no redshift catalog has been published for high  $z$  objects as yet. The HDF-N NICMOS images have been analyzed by Moth & Elston (2002) for purposes partly overlapping with the ones aimed here; eventually, the HDF-S NICMOS field is chosen for the present study.

The HDF-S NICMOS field was formed during the observations of the main field of HDF-S with the WFPC2 camera. The NICMOS camera was operating in a parallel mode, pointing to a slightly different direction in the sky and acquiring data through the NIC-3 camera's broadband  $J$ -,  $H$ - and  $K$ -filters, thereby creating an additional field with an angular area of  $\sim 1$  square arcminutes; its total exposure time matches that of the primary field. The field has also been covered by the WFPC2 camera  $I$ -filter observations (HDF-S Flanking Field 9, Lucas et al. 2003) and more recently, by the

Survey	Camera & filter	$\Delta\lambda^\dagger$ ( $\mu\text{m}$ )	$\lambda_c^\ddagger$ ( $\mu\text{m}$ )	resolution (arcsec)	$t_{\text{exp}}^\#$ (hrs)
Groth Survey	WFPC2, F606W	0.21	0.59	0.1	0.78
Strip	WFPC2, I814W	0.16	0.79	0.1	1.22
Medium Deep Survey	WFPC2, F606W	0.21	0.59	0.1	0.78
	WFPC2, I814W	0.16	0.79	0.1	1.22
HDF-South	WFPC2, F606W	0.21	0.59	0.04	22.6
	WFPC2, I814W	0.16	0.79	0.04	27.9
HDF-South	STIS open mode	0.44	0.59	0.025	7.19
NICMOS field	NICMOS, F110W	0.59	1.12	0.075	30.2
	NICMOS, F160W	0.40	1.65	0.075	35.7

Table 3.1: General information about the observations ( $^\dagger$  passband width;  $^\ddagger$  central wavelength;  $^\#$  total exposure time).

“open mode” observations with the STIS camera. In the latter case, no filter is attached to the front of the camera – the detectable wavelengths are only restricted by the sensitivity of the detector, providing a very broad pass-band, with the central wavelength matching that of the standard  $V$ . The variety of observations at different wavelengths, available for the HDF-S NICMOS field makes this a suitable region for our photometric study.

Regrettably, the  $I$ - and  $K$ -band observations could not be used for the current purposes. The Flanking Field observations did not exploit exposure times long enough for faint objects – they lack of depth. The  $K$  filter images were taken during the “bright” time, i.e. when the telescope was pointed near the bright limb of the earth, resulting in a too high background level.

The remaining three passbands –  $V$ ,  $J$  and  $H$  – have been used for the present study. Again, the images were retrieved from the Space Telescope Science Institute’s archive; their basic properties are listed in Table 1.

Unfortunately, spectroscopic redshifts of galaxies in the HDF-S NICMOS parallel field have not been measured. We had to rely on the photometric redshifts calculated by Yahata et al. (2000). They have used 9-band flux measurements for the calculations, thus these redshifts can be considered sufficiently accurate. The authors’ comparison of their method to spectroscopic measurements indicated a mean redshift deviation  $\Delta z = 0.09$  for redshifts  $z < 2$  and  $\Delta z = 0.29$  within the range  $2 < z < 4$ .

To avoid causing selection effects, we applied no other requirement for

the galaxies than a disk-like morphology. Discrimination between different Hubble types is not a trivial task at high redshifts: in addition to the limitations set by imaging equipment, a considerable fraction of objects may occur in transition stages – protodisks or protospheroids – already at  $1 < z < 2$  (Conselice et al. 2004). For constructing the sample, morphological structure was inspected visually on the basis of  $H$ -band exposures; all galaxies suspected for being disks were included in the sample. In some cases, also the high-resolution STIS  $V$ -band images were checked. The final assurance for the sample to be consisting of only disk galaxies comes from the luminosity profiles, which all exhibit Sérsic index  $n < 2$  and should thus be of a late-type morphology (Andredakis et al. 1995, Ravindranath et al. 2004).

Galaxies showing significant asymmetry or irregular shape were excluded; fitting ellipses to their isophotes would have given rather scattered luminosity profiles (the measured light distribution is very sensitive to the choice of the galactic center position) and their interpretation would not have been straightforward in the context of the present models and analysis. Therefore, possible starburst- and interacting galaxies were rejected as photometrically incomparable to regular disks.

The selection criteria described above finally set a redshift limit at  $z = 2.6$ , beyond which no disk galaxies could be distinguished with acceptable confidence. 22 disks were found in the range  $0.5 < z < 2.6$  for the subsequent analysis. Images of these galaxies are presented in paper III, Fig. 1.

The variety of passbands described above allows us to determine rest-frame optical luminosity profiles, using the STIS observations for redshifts  $z < 1.0$  and NICMOS  $J$  and  $H$  observations for  $1.1 < z < 2.0$  and  $z > 2.1$ , respectively; the mean central rest-frame wavelength thereby becomes 420 nm, roughly corresponding to Johnson  $B$  filter. Color information can be obtained, using STIS and NICMOS  $J$  observations at  $z < 1.1$ , and NICMOS  $J$  and  $H$  bands at  $z > 1.4$  (no galaxies were found at  $1.1 < z < 1.4$ ). The mean central rest-frame wavelengths now become 350 nm and 580 nm, allowing the derivation of  $(U - V)$  color distribution. Note that STIS observations are used for deriving both the  $U$  and  $B$  rest-waveband photometry for the same galaxies. This can be justified by the very wide “passband” of STIS open mode, limited only by the detector sensitivity. A drawback of using such a wide wavelength range lies in the danger of suppressing possible color-features and trends, but it does not introduce or artificially amplify the evolutionary effects.

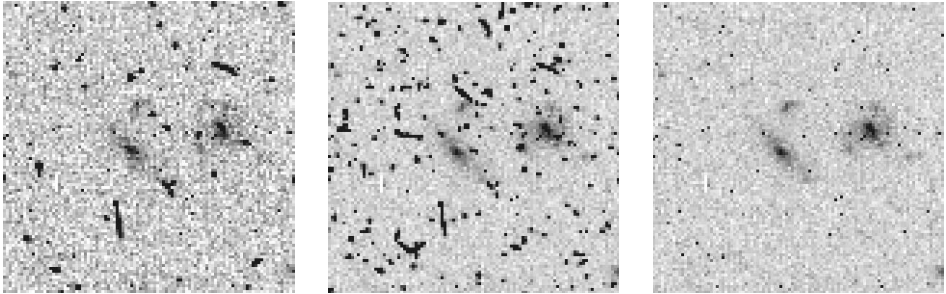


Figure 3.1: Demonstration of the advantages of multiple exposures over a single, correspondingly longer exposure (from left to right): a single exposure; a sum of 4 exposures, identical to an equally longer single exposure; a combined image of 4 exposures, constructed using pixel-by-pixel weighting. Weighted combining enables to eliminate traces of cosmic ray hits.

### 3.3 Processing the original observations

#### 3.3.1 Image reduction

Fully calibrated and processed images (including the pipeline reduction, cosmic-ray removal, dithering and background subtraction) were available for the HDF-S and HDF-S NICMOS fields. The images of the GSS and MDS fields, available at the web-archive, had only experienced the routine pipeline reduction (dark-current and bias removal, shutter shading corrections etc). We carried out the rest of the reduction with the help of the astronomic data handling software IRAF/STSDAS.

Space-born images are usually strongly affected by cosmic rays. Weighted combining with the STSDAS task *Combine* of the multiple images, available for each galaxy in each passband, enabled an effective removal of the traces of cosmic rays, as demonstrated in Fig. 3.1.

For estimating absolute magnitudes and colors of galaxies, accurate background subtraction has to be conducted. However, in the case of faint objects, background level determination often becomes a complicated task, due to background variations within an exposure, crowded field and low signal-to-noise ratio. We tested three different methods for background estimation: the most common way of finding the mean intensity value of several empty-looking regions around each galaxy; a visual inspection of the cut graphs of pixel rows; using radially averaged galaxy luminosity profiles. The latter approach is based on the fact that outer edges of the measured luminosity profiles are sensitive to over- or under-subtraction of



the background (Binney & Merrifield 1998, pp. 175-176). In general, all three methods gave close results, but perhaps owing to minimal human intervention, scatter of the results of the first procedure were the smallest.

Careful inspection revealed that in general, the background levels of the original HDF-S NICMOS images were slightly over-subtracted and also varying across the field, ranging from -0.00015 to 0 counts per second for the STIS field and from -0.00005 to 0.00002 counts per second for the NICMOS images.

### 3.3.2 PSF deconvolution

When a point source is observed with a telescope, its image will not be a point any longer. Diffraction inside the telescope, leakage between neighboring pixels of CCD-matrixes, focus offset and other effects cause point-spreading, which can seriously distort both stellar and galactic images. For example, the more concentrated luminosity of bulges of distant spiral galaxies may be smeared over a significant part of the whole galactic image, leading to an incorrect photometry and even a wrong Hubble type determination. Radial shape of the distortion, called the point-spread-function (PSF), varies with position across the field of view and may also be time-dependent. Despite these complications, PSF can be determined relatively accurately and its effect can be reduced or removed via a non-linear deconvolution process. On the other hand, incorrect deconvolving may lead to even more serious distortions.

For the HST's optical detectors, the PSF can be and has been studied thoroughly, and the TinyTim software can well be used for generating a synthetic PSF for an exposure taken at a given time, at a given location on the field of view. This procedure would then be followed by a deconvolution with, for example, the Lucy-Richardson algorithm within the STSDAS software package. This is exactly what we have done with the optical images taken with the WFPC2 and STIS cameras.

The effect of point-spreading is strongest for the NIC-3 camera, which is due to the detector being slightly offset of the focus. Moreover, PSFs of all NICMOS cameras are considerably time-dependent and their universal determination does not guarantee a good image restoration (a more detailed description of the problem can be found in the HST Data Handbook for NICMOS). A better deconvolution is achieved by using stellar images from the same exposure, ensuring that all distorting effects are being properly accounted for. Fortunately, suitable stars with unsaturated images are present on exposures of the HDF-S NICMOS field and they have been used

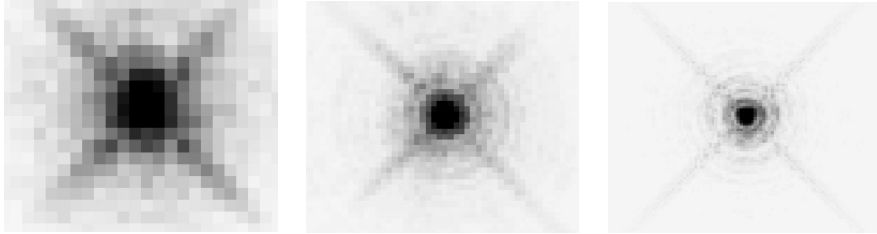


Figure 3.2: Comparison of point source images as modeled by TinyTim software for (from left to right): NIC3, WFPC2 and STIS camera of the Hubble Space Telescope. The wider point-spread-function of NIC3 camera is primarily caused by a slight focal offset of the detector. The images are calibrated to identical logarithmic luminosity scale and are  $6 \times 6$  arcseconds in size.

as model PSF-s in the present study. A comparison of the PSFs of the NIC3, WFPC2 and STIS cameras is presented in Fig. 3.2. The impact of PSF-deconvolution on some of the surface brightness profiles of the current sample galaxies is shown in paper I, Fig. 2 and paper II, Fig. 2.

### 3.3.3 Isophote fitting

In order to measure radially averaged surface-brightness distribution, elliptical isophotes were fitted to PSF-deconvolved galactic images. Task *Ellipse* within STSDAS was used for performing such an operation. Fitting ellipses to faint and noisy images may lead to improper solutions, thus the task was run interactively, manually guiding the program to find the initial parameters (center coordinates, mayor-axis directions, etc). Objects not considered to belong to a galaxy under investigation were masked out. In cases of doubtful and scattered results, several runs of the fitting task were performed. The median values of separate runs were used for the construction of the final luminosity profiles.

PSF-deconvolution process may rise noise level and also distort the outer edges of galaxies. Thus in cases of very low signal-to-noise ratio, luminosity profiles of non-deconvolved images were used for determining the outer edges of the final profiles.

For measuring color profiles, it is important to avoid artificial effects arising from differences in the resolution and PSFs of the exposures taken with different cameras. On the other hand, deconvolving the point-

spreading may cause additional uncertainties, thus it is more reasonable to process all the images to match the ones suffering from the worst PSF. In the web-archive, STIS images already calibrated to match the resolution and the PSF of the NICMOS camera were available for the HDF-S NICMOS field. The task *Ellipse* was first run on a summed rest-frame ( $U + V$ ) image, thereby determining the positional parameters for elliptical isophotes of each galaxy in a least discriminative way. The acquired ellipse geometries and positional parameters were subsequently used for fitting the  $U$  and  $V$  images; the corresponding ( $U - V$ ) color profiles could thus be created.

### 3.3.4 Photometric calibrations

Prior to conversion of the flux into standard magnitudes, the absorption inside the Galaxy was corrected for. According to Schlegel et al. (1998), the corrections remained below 0.1 magnitudes (with one exception). No attempt was made to compensate for the intrinsic absorption of the galaxies or dust attenuation in the Universe. These corrections are not well-known for objects at such high redshifts.

The conversion of the measured flux into some standard filter magnitudes (the Johnson  $UBVRI$  for example) is usually a routine procedure for a given detector, provided the corresponding calibration constants are available, determined by observations of some standard object with a known spectrum. For the filters of the HST's WFPC2 camera, calibration constants and formulae have been derived by Holtzman et al. (1995). In the case of distant sources, the redshift of the spectra has to be taken into account. The corresponding conversion is called the k-correction. By definition (Oke & Sandage 1968), k-correction relates the observed energy flux density  $F(\lambda)$  to the energy flux density of an object at rest  $F(\lambda/(1+z))$ :

$$K_i(z) = -2.5 \log(1+z) - 2.5 \log \left[ \frac{\int S_i(\lambda) F(\lambda) d(\lambda)}{\int S_i(\lambda) F(\lambda/(1+z)) d(\lambda)} \right], \quad (3.1)$$

where  $K_i(z)$  is the k-correction of an object at redshift  $z$ , observed through a filter  $i$ ,  $S_i(\lambda)$  is the sensitivity function of the filter and  $d(\lambda)$  is its bandwidth. For galaxies at cosmological distances, k-correction becomes large and also more uncertain. Therefore, it is often more sensible to convert the measured luminosity into magnitudes of a bluer standard filter pass-band than the one of the actual observation. This can be done accurately only if the spectrum of the object is known.

For the galaxies used for mass-modeling, k-corrections were conducted according to van Dokkum & Franx (1996) and Kelson et al. (2000). Synthetic spectra were taken from the paper by Coleman et al. (1980), the relation between the Johnson magnitudes and AB-magnitudes from Frei & Gunn (1994). Johnson  $B$  was found to be the nearest rest-frame standard pass-band for the transformations. For the closest galaxy at  $z = 0.15$ ,  $I$ -filter flux was used for the conversion, while the  $V$ -band suited better for the remaining six galaxies.

Necessary k-corrections existed for transformations from neither the STIS open mode nor the NICMOS passbands; we had to calculate them. In the calculations we relied on the synthetic spectra of Sb galaxies (as a mid-way between S0 and Sc galaxies), constructed by Bicker et al. (2004) according to their chemical evolution models. In these spectra, effects of redshifting as well as evolution had been taken into account. Our task was to find a relation for the observed flux and the redshifted standard  $U$ ,  $V$  or  $B$  filter flux for each set of cameras, filters and redshifts. The throughput curves of the NICMOS filters and STIS clear imaging were taken from the NICMOS and STIS Instrument Handbooks, respectively. The calculations were conducted according to formula

$$K_i = -2.5 \log \left[ \frac{FWHM_0 \times S_0 \times F_0}{FWHM_i \times S_i \times F_i \times (1+z)} \right], \quad (3.2)$$

where  $M_i$  is the measured magnitude,  $FWHM_i$  the bandwidth of the actual filter used,  $S_i$  the mean value of the redshifted synthetic spectrum within the redshifted throughput range of the filter and  $F_i$  is the mean throughput of the filter within its FWHM. “0” denotes the corresponding values for the standard filter and spectrum at rest.

Due to the available choice of filters, the actual wavelength-shifts along the spectra remained small. In the final k-corrections (typically around 0.4–0.7 magnitudes for both rest-frame  $B$ -luminosity and  $(U - V)$  color), differences in passbands’ widths and throughputs are dominating.

For estimating uncertainties of these k-corrections, inaccuracy of our Hubble type classification and the population synthesis models were considered. It was difficult to estimate the latter precisely, because no actual uncertainties of chemical evolution models are available; we made a rough estimate on the basis of deviations of synthetic spectra calculated by different authors. In turn, these uncertainties are amplified by differences between the widths and shapes of the actual and the target rest-frame passbands. Uncertainties of the synthetic spectra at higher redshifts are larger than at lower redshifts, but our estimate for the final uncertainties

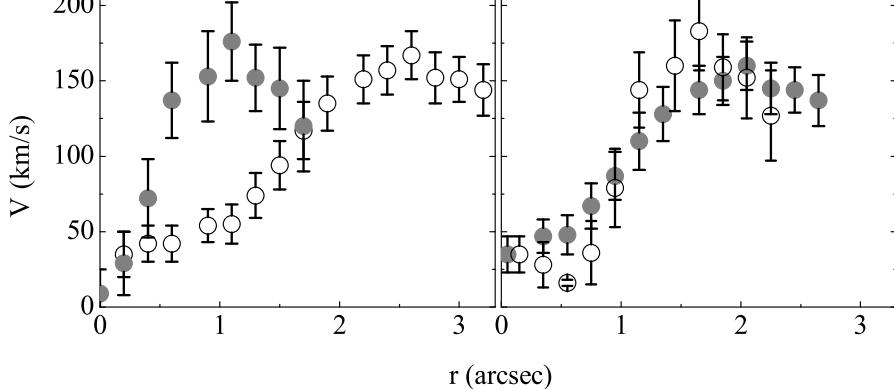


Figure 3.3: Left: the rotation curve of the galaxy GSS 104-4024, as measured by Vogt et al. (1996), with the receding side (filled circles) folded over the approaching side (empty circles). Right: the same rotation curve after refolding with respect to new  $r(0)$  and  $V(0)$ .

remain comparable (0.25–0.45 mag) over the redshift range. This is because of the spectra being stretched as  $(1+z)$  with respect to the filter passband on one hand, thus enabling a more exact determination of the flux, and because of the usage of the wide-band STIS imaging at the tricky UV-region for lower redshift galaxies on the other hand, which can not be very accurate. The step of determining the actual flux according to the synthetic spectra dominates in the estimates of the uncertainties of the final color measurements.

### 3.3.5 Recalibrating the rotation curves

In principle, it should be possible to determine the exact location of the center coordinates  $V_0$  and  $r_0$  of a rotation curve according to the redshift of the galaxy and the slit position of the spectrograph. In practice, and especially in the case of distant galaxies, the measured rotation curve needs additional shifting along  $V$  and  $r$  axes, respectively, in order to minimize the difference between the rotation measured in opposite directions from the center (Persic & Salucci 1995). The original rotation curves constructed by Vogt et al. (1996) needed this kind of treatment<sup>1</sup> (Fig. 3.3, left panel). To conduct such shifting, the rotation curves have been refolded with respect to other  $V_0$  and  $r_0$  than the original values (Fig. 3.3, right panel). The desired result was achieved by varying the center coordinates until the deviations between the velocities of the approaching and the receding side were the smallest.

<sup>1</sup>Thanks to Dr. Paolo Salucci for drawing our attention to this aspect.

In the literature, these rotation curves are presented without showing the corrections for the slit width. Slits used for the detection of spatially resolved spectra of high redshift galaxies are commonly wider than the scale length of the whole galaxy and the measured velocity is actually an integration across the galactic image – an effect called “beam smearing”, according to an analogy with radio observations. In these cases, synthetic RCs are constructed, where such effects are already accounted for. These RCs are then fitted to the measured values; thus the actual velocities are significantly higher than seen in the graphs. Without the necessary information, we could not derive the actual velocities; instead, we recalibrated the rotation curves to reach the corresponding  $V_{max}$ , presented in the source papers. Such a correction is justified at outer radii, but it does not restore the actual rotation curves near the central regions. Anyway, accurate measurements of the velocities near the centers of distant galaxies still have to wait until telescopes larger than currently available are constructed.

### 3.4 Modeling

The complex nature of disk galaxies can be handled more easily, if its observable properties are considered to result from a superposition of sub-systems and stellar populations. This allows a more accurate classification of the galaxies, but also enables to study and compare the properties of individual components. For example, the luminosity distribution is often split into the contribution of a bulge and a disk component, but with the presence of accurate photometry, much more elaborate decomposition can be conducted, distinguishing also a bar, a thin disk and a thick disk, an inner disk, a halo etc. In the case of distant galaxies, imaging limitations usually allow to discriminate between maximally two visible components - a bulge and the disk.

#### 3.4.1 Sérsic approximation for luminosity distribution

The radial surface density distribution (also the observed surface brightness distribution) of both a bulge and a disk components of a disk galaxy can usually be fitted well by the universal law (Sérsic, 1968):

$$I(r) = I(0) \cdot \exp[-b_n(r/r_e)^{1/n}] \quad (3.3)$$

In this formula,  $r$  is distance along the galactic major axis,  $r_e$  is the effective radius containing half of the total luminosity,  $n$  is the shape parameter,

setting the curvature of the profile and  $b_n$  is a normalizing constant, dependent on  $n$ , calibrated to keep  $r_e$  the half-light radius. Usually,  $n = 2-4$  for spheroids and  $n \approx 1$  for disks is a good approximation.

To determine  $b_n$ , either gamma functions or integral equations have to be numerically solved. In general, the requirement

$$\int_1^\infty e^{-b_n x^{1/n}} x dx = \int_0^1 e^{-b_n x^{1/n}} x dx \quad (3.4)$$

has to be satisfied, where  $x = r/r_e$ . This condition can be solved analytically for a few certain  $n$  values only. Therefore, often  $b_n = 1.9992n - 0.3271$  (Capaccioli 1989) or other simplification formulae are used (e.g. Prugniel & Simien 1997, Moriondo et al. 1998, Ciotti & Bertin 1999). They can be very successfully applied at  $n$  values above  $n \approx 0.7$ , but if lower  $n$  values (i.e. more curved profiles) are present, these simplifications start to mislead. Within the current sample,  $n$  values as low as  $n \approx 0.5$  appeared. We therefore constructed our own approximation:

$$b_n = 2n - \frac{1}{3} + \frac{1}{65n}, \quad (3.5)$$

which can well be used down to  $n = 0.1$ . Comparison of this approximation with the approximations by Capaccioli (1989) and Ciotti & Bertin (1999) is given in Fig. 3.4. The actual  $b_n$  values, found by numerical integration, are also shown (thick gray line). To emphasize deviations at small  $n$  values, logarithmic scale has been used in the figure.

We have fitted the Sérsic distribution to the luminosity profiles of the galaxies used for purely photometric sample, thus enabling a comparison with parameters from other studies. No attempt has been made to split the luminosity profiles into separate contributions by the components – bulges of high-redshift disk galaxies are often indistinguishable or are distorted by PSF and such discrimination might lead to systematically different disk parameters at different redshifts. As a tool for fitting surface brightness distribution, the Sérsic law has a purely empiric background. Starting from a spatial density distribution and projecting it along the line of sight would be a more physical method, allowing a straightforward comparison with kinematic data and thereby enabling the construction of self-consistent models for mass distribution.

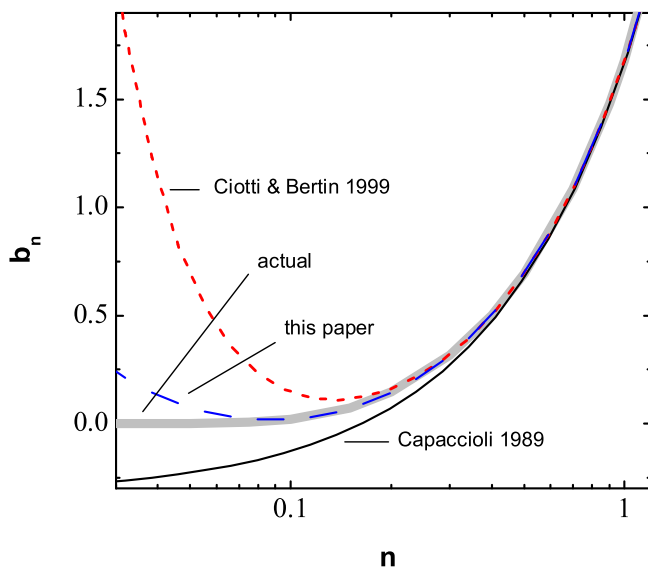


Figure 3.4: Normalizing parameter  $b_n$  in the Sérsic formula (3.3) at low  $n$  values. Comparison of our approximation (3.5) with numerically calculated actual values, together with approximations from the literature.



### 3.4.2 Luminosity distribution from space density distribution

Fitting model surface density distributions to galactic luminosity profiles is merely an empirical method, without a physical connection with the actual space density distribution. A more flexible and physically justified method would be starting from a space density distribution law and projecting it along the line of sight, thus deriving the corresponding surface brightness distribution. In addition, constructing a rotational velocity curve of radially symmetric components would now become a rather trivial task (see the next section).

We have applied such a method to the galaxies of the mass distribution sample, using space density distribution of the very general form (Einasto 1969)

$$\rho(a) = \rho(0) \exp[-(a/(ka_0))^{1/n}]. \quad (3.6)$$

where  $\rho(0) = hM/(4\pi qa_0^3)$  is the central density and  $M$  is the component mass;  $a = \sqrt{R^2 + z^2/q^2}$ , where  $R$  and  $z$  are two cylindrical coordinates.  $q$  is the axial ratio,  $a_0$  is the harmonic mean radius which characterizes rather well the real extent of a component, independently of the parameter  $n$ . Coefficients  $h$  and  $k$  are normalizing parameters, depending on  $n$ , which allows to vary the density behavior with  $a$  ( $k$  is similar to  $b_n$  in the Sérsic formula). The definition of the normalizing parameters  $h$  and  $k$  and their calculation is described in Tenjes et al. (1994). Equation (3.6) allows a sufficiently precise numerical integration and has a minimum number of free parameters.

The density distributions for the bulge and the disk are projected along the line of sight, divided by their mass-to-luminosity ratios  $f$  and their sum gives us the surface brightness distribution of the model

$$L(A) = 2 \sum_{i=1}^2 \frac{q_i}{Q_i f_i} \int_A^\infty \frac{\rho_i(a) a da}{(a^2 - A^2)^{1/2}}, \quad (3.7)$$

where  $A$  is the major semiaxis of the equidensity ellipse of the projected light distribution and  $Q_i$  are their apparent axial ratios  $Q^2 = \cos^2\gamma + q^2 \sin^2\gamma$ . The angle between the plane of the galaxy and the plane of the sky is denoted by  $\gamma$ . The summation index  $i$  designates two visible components, the bulge and the disk.

Luminosity distribution, derived with this method, is somewhat different from the Sérsic distribution. Nevertheless, if fitted to a real density distribution, the main parameters ( $n$ ,  $a_0 \approx r_e$ ) remain close to those acquired

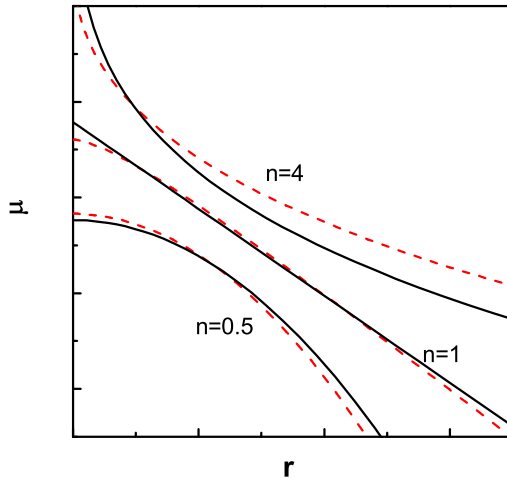


Figure 3.5: Comparison of the Sérsic surface brightness distribution (solid lines) and a distribution, derived from the space density distribution Eq. 3.6 (dashed lines) at different  $n$  values. Surface brightness value  $\mu$  and radius  $r$  are given in the same relative units for both distributions. No rescaling has been conducted to match the curves.

from the Sérsic law. Comparison of these two distributions at different  $n$  values is given in Fig. 3.5. Surface brightness value  $\mu$  and radius  $r$  are given in the same relative units for both distributions. No re-scaling has been conducted for matching the distributions; the fit has been achieved by preserving the same total luminosity. Note that a perfectly exponential distribution, corresponding to Sérsic law with  $n = 1$ , can not be attained with the distribution 3.6.

### 3.4.3 Self-consistent mass distribution modeling

A proper mass distribution model of a realistic disk galaxy has to be in correspondence with its observed luminosity distribution as well as with its spectroscopically determined internal kinematics. If such a model is to be created, the luminosity distribution would often be taken as the bases, from which circular velocity distribution can be derived, using the Bessel functions (Freeman 1970). For model construction, usually a 3-dimensional, rotationally symmetric shape is assumed for the galaxies.

Rotation curves can be derived directly from luminosity distribution only with the assumption of an infinitely thin disk and an exponential sur-

face density distribution. For spherically symmetric systems, an expression for circular velocity has been derived from the Sérsic luminosity distribution with an integer index  $n$  (Mazure & Capelato 2002). The same can be done only for a few cases of axial symmetry (Binney & Tremaine 1987).

Alternatively, an analytic form for space density distribution may be used as the bases of the calculation of model parameters. Model distribution is constructed either empirically (e.g. Casertano 1983, van den Kruit et al. 2001) or can be derived from an analytic expression of gravitational potential (Miyamoto & Nagai 1975).

Depending on the quality and amount of the data at hand, models consisting of multiple components can be built. In addition to the luminous components, a realistic model should include a dark matter halo. Model rotation curves are calculated as resulting from the superposition of all components and are subsequently fitted to the observed rotation; thereby mass-to-light ratios ( $M/L$ ) can be determined.  $M/L$  is either considered constant over each component (e.g. Casertano 1983, Carignan 1985, Palunas & Williams 2000, Dutton et al. 2005, Kregel & van der Kruit 2005) or is allowed to vary (e.g. Takamiya & Sofue 2000, Simon et al. 2003).

In the present study, analytic space-density distribution (3.6) is used as the bases and  $M/L$  ratio is considered uniform over each component. Model rotation curves can now be simply determined from the rotation law

$$v_i^2(R) = 4\pi q_i G \int_0^R \frac{\rho_i(a) a^2 da}{(R^2 - e_i^2 a^2)^{1/2}}, \quad (3.8)$$

$$V^2(R) = \sum_{i=1}^3 v_i^2(R), \quad (3.9)$$

where  $G$  is the gravitational constant,  $e = \sqrt{1 - q^2}$  is eccentricity, and  $R$  is the distance in the equatorial plane of the galaxy. The summation is over all the components, including the dark matter halo. Discussion about dark matter distribution in general and the one used here will be presented below.

### 3.4.4 Dark matter distribution

In the literature, several forms of density distribution have been proposed for dark matter halos. From the observed rotation curves, the “cored” type of distributions have been deduced, where at small radii, density asymptotically approaches a constant value,  $\rho(0)$ . For example, Burkert (1995)

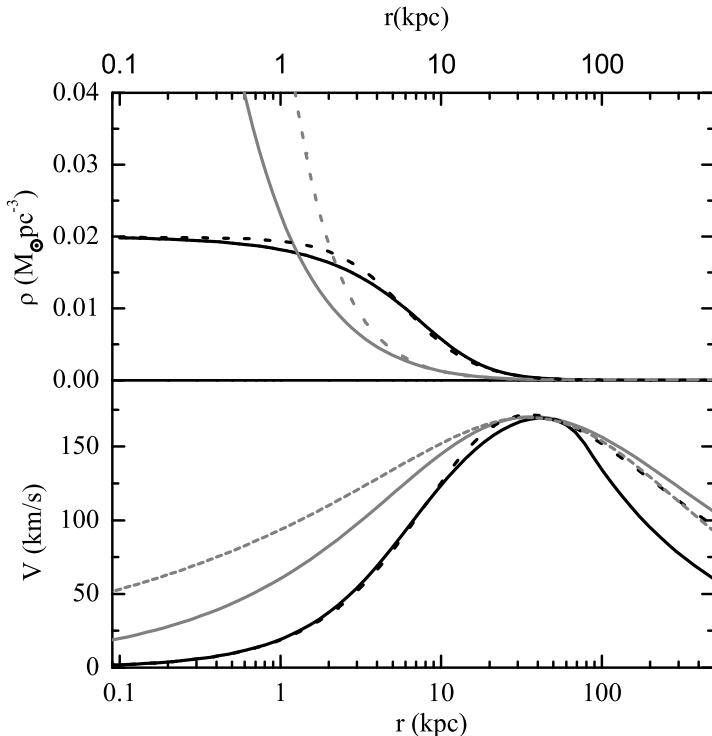


Figure 3.6: Upper panel: density distributions for dark matter halos as seen in numerical simulations by Navarro et al. (1996; gray solid line) and Burkert et al. (1999; gray dotted line) and as fitted to actual galaxies: Burkert (1995; black dotted line) and in the present work (black solid line; see text). Lower panel: the corresponding rotation curves.

has studied low surface-brightness galaxies and approximated the dark halo component with the following distribution:

$$\rho(r) = \frac{\rho_0 r_0^3}{(r + r_0)(r^2 + r_0^2)} \quad (3.10)$$

Black dashed line in Fig. 3.6 shows the behavior of this distribution and the circular velocity curve initiated by its potential. In contrast, especially at inner radii, numerical simulations of  $\Lambda$ CDM develop halos with density increasing infinitely towards the center. The pioneering work by Navarro et al. (1996) showed such “cuspy” profiles to be universal over a wide range of mass-scales. Their fitting formula

$$\rho(r) = \frac{\rho_s}{(r/r_s)[1 + (r/r_s)]^2} \quad (3.11)$$

is shown with solid gray line in Fig. 3.6. More recent simulations with higher mass resolution have produced even steeper profiles (e.g. Moore et al. 1999; gray dotted line). The limited extent and spatial resolution of the rotation curves and the lack of velocity dispersion measurements in the inner regions of the galaxies of the present sample does not allow to favor any particular dark matter density behavior. In general, observational data suggest that “cored” distributions are more favored, thus one of the form

$$\rho(a) = \begin{cases} \rho(0)[1 + (\frac{a}{a_c})^2]^{-1} - [1 + (\frac{a^0}{a_c})^2]^{-1} & a \leq a^0 \\ 0 & a > a^0. \end{cases} \quad (3.12)$$

has been used for modeling here. In this formula,  $a^0$  is the outer cutoff radius of the isothermal sphere and  $a_c = ka_0$ , with  $a_0$  being the core radius and  $k$  being a normalizing parameter, see Tenjes et al. (1994). Black solid line represents this distribution in Fig. 3.6.

### 3.4.5 Model fitting. Limitations of the final models.

Model fitting was carried out with the help of special software, created by Dr. Urmas Haud.

Galaxies were modeled as consisting of three components: a bulge, a disk and a dark matter halo. The axial ratios of the components were kept fixed, taking  $q = 0.7$  for the bulge and  $q = 0.1$  for the disk, according to analogy with the near-by galaxies. The subsequent least-squares approximation process determined the model parameters  $a_0$ ,  $L_B$ ,  $M$  and  $n$  for bulges and disks. Details of the least squares approximation and the general modeling procedure have been described by Einasto & Haud (1989), Tenjes et al. (1994, 1998).

The modeled luminosity distributions could be fitted to the actual profiles with very small deviances, generally well below 0.1 mag/arcsec<sup>2</sup>. Fitting of the rotation curves was much less straightforward and the derivation of masses involved remarkable uncertainties, due to the aspects described below.

Fig. 3.7 shows that without any additional data, the correct balance between the contributions of luminous and dark matter to the RC remains unknown: it is possible to achieve a fit using either just the share of the luminous components or the dark matter component, thus additional information or assumptions have to be applied. The estimation of the separate contributions by luminous and dark matter is difficult even for local galaxies, as the actual  $M/L$  of luminous matter is not well known (e.g. Dutton et al. 2005). With the presence of multicolor photometry, an independent

$M/L$  determination can be attempted (Bell & de Jong 2001). Otherwise, the maximum disk assumption is most commonly used for breaking the degeneracy between luminous and dark matter (e.g. Palunas & Williams 2000), providing an upper limit for  $M/L$  of disks and an approximate minimal central density value for DM halos. Such a method has been followed here as well.

The RCs of the modeled galaxies have a rather small extent (less than 20 kpc from center). Without any additional information about the dynamics of these galaxies at larger galactocentric radii, the amount of dark matter had to be assumed from analogy with nearby galaxies. In general, RCs of disk galaxies remain nearly flat at least up to 30 kpc, forming a velocity plateau at  $\sim 1.5 - 2R_{opt}$  (Persic et al. 1996, Sofue & Rubin 2001), so the dark halo mass was raised to such a level which minimally provided a plateau at radii beyond the observed data points. We thereby assumed that the observed RCs had reached the actual maximal rotation values and would remain roughly constant further on. The outer cutoff radius of the DM component was fixed at  $a^0 = 5a_0$ , also on the basis of the structure of nearby galaxies. This value influences the behavior of RCs only in the extreme outer regions and does not affect the results of the present analysis.

Individual parameters of DM halos cannot be determined uniquely by the present method. It is possible, for example, to increase the halo mass, if its radius is increased simultaneously. A parameter that can be determined reasonably well, however, is the central density of the dark halo  $\rho(0) = hM/(4\pi qa_0^3)$ .

Without observational data about velocity dispersions in the central regions of the galaxies, we could calculate only circular velocities (Eqs. 3.8, 3.9). In galactic dynamics, the difference between the circular and rotational velocities is known as the asymmetric drift; it is mainly a function of velocity dispersions. Typical emission-line dispersions in disk galaxies at intermediate redshifts are 30 – 100 km/s or even more (Im et al. 2001, Erb et al. 2003). In turn, circular velocities may be underestimated as a result of low spatial resolution caused by slit width used for spectroscopy (Swaters et al. 2000, van den Bosch et al. 2000, Blais-Ouellette et al. 2004). Thus, within the central  $0.5'' - 0.7''$ , modeled velocities must be significantly higher than the observed rotation and the actual masses of bulge components cannot be determined uniquely. However, assuming the bulge of a galaxy to be populated by stars from an older generation than the disk, it is possible to get the approximate lower limit for bulge mass by fixing its  $M/L$  ratio at the level of the disk component.

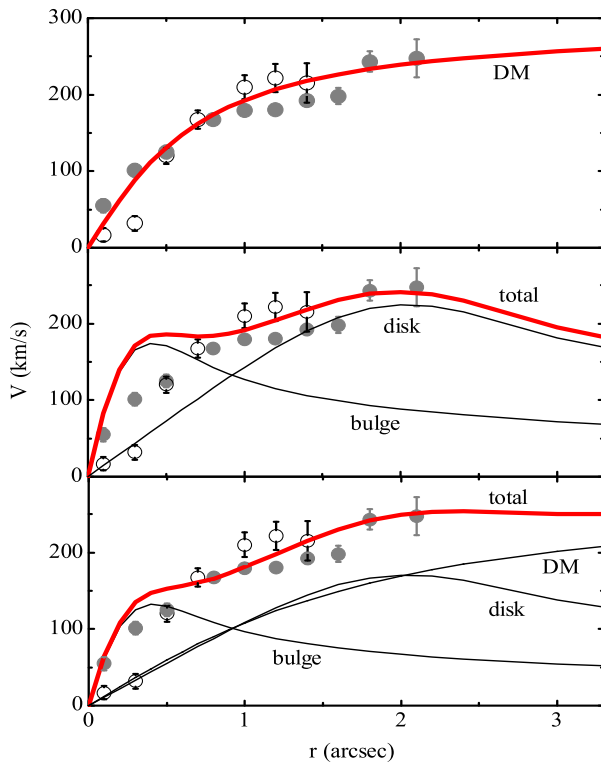


Figure 3.7: Measured rotation of the galaxy 094-2210, overplotted with different models. Upper panel: a pure dark matter halo fit. Middle panel: a fit with the visible components. Due to technical limitations of rotation curve measurements, both can provide a satisfactory fit; in order to determine mass-to-light ratios, additional assumptions have to be applied on the basis of local galaxies. Lower panel: a maximum disk model with an equal mass-to-light ratio for the bulge and the disk and a velocity plateau at the outer regions.

For the reasons presented above, no actual masses for neither bulge nor DM mass could be derived, while disk mass should be considered as the upper limit and central density of the DM halos  $\rho(0)$  as the lower limit in each case.



# Chapter 4

## Results and discussion

In this chapter, general results and trends will be presented and discussed. More specific results for individual galaxies can be found in papers I, II and III. Three examples of galaxies from the photometric sample together with the derived luminosity curves and color profiles are presented in Fig. 4.1.

### 4.1 Luminosity profiles

The luminosity distributions and model fits are presented in Figs 2 and 3 of paper I, Figs 2, 3 and 4 of paper II and Fig. 2 of paper III. In many cases, a poor fit was achieved with a simple exponential profile  $I(r) \sim \exp(r/r_e)$ , which corresponds to Sérsic index  $n = 1$  and is commonly used for approximating local disks; several galaxies of the present sample showed much steeper luminosity decrease with radius. In contrast, both Sérsic distribution and the distribution, derived from the spatial density distribution model (3.6) gave good fits if  $n < 1$  was used. The mean deviations of the models from the measured surface brightness within a disk scale length ranged from 0.005 to 0.4 magnitudes per square arcsecond, dependently on the redshift, the camera used for the observation and the exposure time.

Rapidly decreasing luminosity distribution has also been obtained by Moth & Elston (2002) for distant galaxies in the HDF North field. Such curved profiles might indicate the effect known as disk truncation, discovered in studies of local edge-on disk galaxies (de Grijs et al. 2001, Pohlen et al. 2002); more recently, Pérez (2004) and Trujillo & Pohlen (2005) have shown that truncated disks are common at higher redshifts. Sometimes a double-exponential model profile is fitted to this kind of distribution (Pohlen et al. 2002, Pérez 2004). The physical background of disk trun-

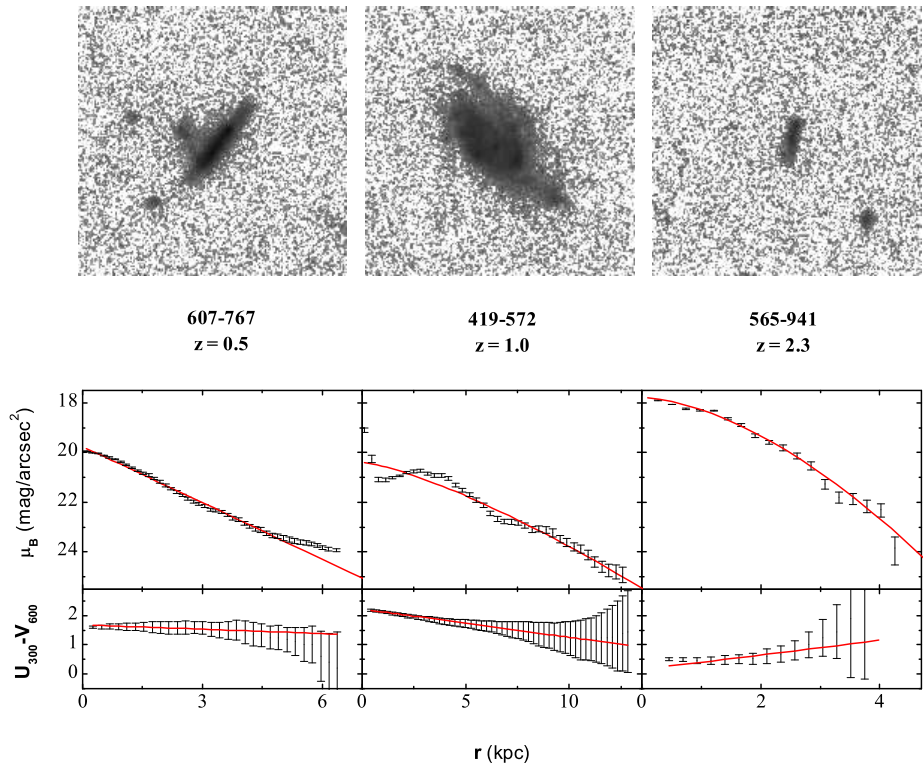


Figure 4.1: Examples of galaxies from the photometric sample and the corresponding  $B$ -profiles with Sérsic fits and  $(U - V)$  color profiles with linear fits. Galaxy 607-767 shows an exponential luminosity profile, flattening at the outer edge and a roughly constant color profile. Galaxy 419-572 has a clear signature of spiral pattern in its luminosity profile and a blueing color profile (negative color gradient). 565-941 is a very compact galaxy with a truncated luminosity distribution and a reddening color profile (positive color gradient).

cation has not become clear as yet (see e.g. Sasaki 1987 and de Grijs et al. 2001 for more discussion about the origin of this phenomenon). In contrast to these truncated disks, some galaxies of the present sample have profiles flattening at the outer edges (for example 607-767, 708-695, 380-1027, 353-444; see paper III, Fig. 2). Similar luminosity distributions have been measured near  $z = 1$  for gamma-ray burst-selected disks (Conselice et al. 2005b) and up to  $z = 3$  for large disks in the HDF-South primary field (Labbé et al. 2003). Erwin et al. (2005) have found a significant proportion of local barred S0-Sb galaxies with flattening profiles, which they call “anti-truncated” disks. They claim that, at least in several cases, this effect might be caused by interactions. Observations of interacting galaxies (Chitre & Jog 2002) and numerical simulations (Bournaud et al. 2005) have demonstrated the ability of mergers to smear out the outer parts of luminosity profiles. In the case of our sample, visual companions are present for all the noted four galaxies, thus interactions may have a role in the development of such flattening here as well. The companions have been masked prior to ellipse fitting, therefore the luminosity of the companions cannot be responsible for the effect. Considering the possibility of merger origin, the tendency of luminosity profile flattening of disks to be common at higher redshifts matches well with the  $\Lambda$ CDM-cosmology, which predicts a higher merger fraction before  $z \approx 0.5$ .

The mean value of the distribution shape parameter (the Sérsic index)  $\langle n \rangle = 0.5$  for the 7 galaxies used for mass modeling and  $\langle n \rangle = 0.85$  for the 22 galaxies used for photometry is a noteworthy deviation. This could be a result of the small size of the samples or might result from selection effects, favoring luminous galaxies with regular kinematics, but no firm conclusions can be made as yet.

## 4.2 Disk sizes

In Fig. 4.2, size evolution of the present sample is shown. The uncertainties of the size estimates were derived by varying  $r_e$  while fitting the Sérsic law within the error bars of the surface brightness profiles.

Starting from the locally observed Universe and modeling galactic evolution backwards, Bouwens & Silk (2002) have derived a scaling relation  $r(z)/r(0) = 1 - 0.27z$  for the  $B$ -band radius. The long-dashed line in Fig. 4.2 shows this relation. A least-squares linear fit to our sample yields  $r_e(z) = r_e(0) = 1 - 0.26z$  (solid line). Here, the median value of Sérsic half-light radii  $\langle r_e \rangle \approx 4.2$  kpc for late-type galaxies from the SDSS survey (Shen

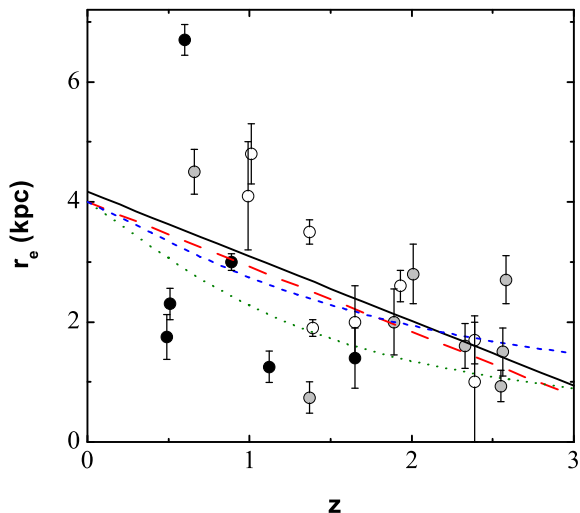


Figure 4.2: Effective radius  $r_e$  as a function of redshift for the photometric sample galaxies. Open circles stand for galaxies with absolute luminosity  $M_B < -20$  mag, gray circles for  $-19 \text{ mag} < M_B < -20$  mag and black circles for  $M_B < -19$  mag. Solid line shows a least-squares linear fit to the current sample; long-dashed line is the relation derived by Bouwens & Silk (2002), see text; dotted and short-dashed lines give the relations  $r_e \sim H(z)^{-1}$  and  $r_e \sim H^{-2/3}(z)$ , respectively.

et al. 2003) has been used as the value for  $r_e(0)$  (considering the median absolute luminosity of the present sample). It is seen that the model developed by Bouwens & Silk (2002) fits our data rather closely. The present result is also consistent with the small  $r_e$  values found for UDF galaxies by Elmegreen et al. (2005).

On the other hand, galactic size evolution has been predicted from simple models of the hierarchical structure formation scenario and an approximate scaling with disk formation time has been derived:  $r_e \sim V_{vir} = H(z)$ , where in the case of  $\Omega_0 = 1$ ,  $H(z) = H_0[\Omega_m(1+z)^3 + \Omega_L]^{1/2}$  (Mo et al. 1998). From the observational point of view, Ferguson et al. (2004) found the scaling of  $r_e \sim H^{-1}(z)$  to give a good fit to their sample of galaxies at a redshift range  $z = 1.5 - 5$ , while Trujillo et al. (2005) achieved a better fit with  $r_e \sim H^{-2/3}(z)$  for galaxies at  $z = 0.3 - 2.5$ . The relations  $r_e \sim H^{-1}(z)$  and  $r_e \sim H^{-2/3}(z)$ , scaled with  $r_e(0) = 4.2$  kpc, are also shown in Fig. 4.2, as dotted and short-dashed lines, respectively. The former shows a decrease

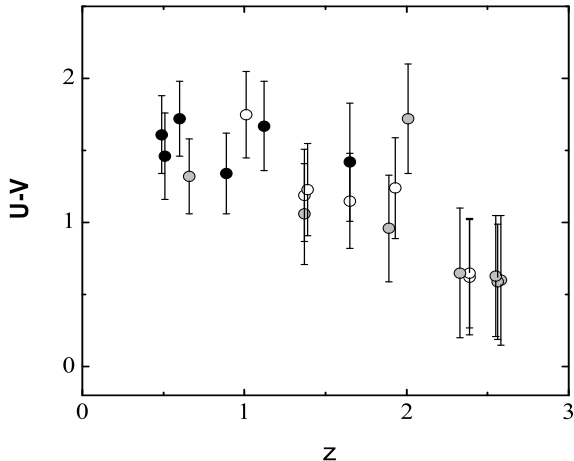


Figure 4.3: Rest frame  $(U - V)$  color as a function of redshift for the photometric sample galaxies. Designations are the same as in Fig. 4.2.

significantly faster than that of the present sample. However, it must be kept in mind that the theoretical relation uses disk formation redshift instead of the observed redshift for scaling. Further more, in contrast to the present sample and the literature referred to above, Ravindranath et al. (2004) and Cassata et al. (2005) detected no significant evolution of galaxy sizes with redshift at all in a thorough study of galaxies at  $z \leq 1.2$ .

### 4.3 $(U - V)$ colors

The rest-frame  $(U - V)$  color profiles of the photometric sample galaxies are presented in paper III, Fig. 2. In Fig. 4.3,  $(U - V)$  color as a function of redshift is plotted. The color shows a mild decrease (i.e. blueing) up to  $z \approx 2$ , followed by a notable drop by roughly 0.7 mag by  $z \approx 2.5$ . At lower redshifts, the dependence can be compared to the Groth Survey sample studied by Weiner et al. (2005), for which a very slight, if any, decrease of  $(U - B)$  was detected for late-type galaxies in the redshift range  $z = 0 - 1.5$ . The notable drop of the  $(U - V)$  values at  $z \approx 2$  cannot be due to a miscalibration – a uniform set of filters and calibrations has been used for the redshift range  $z = 1.4 - 2.6$  (see Sects 3.2 and 3.3.4). However, if the redshift estimate is incorrect by more than  $\sim 10\%$ , the misinterpreted location of the redshifted Lyman jump at 4000 Å could be

a reason for false color estimates at  $z \approx 2$ . If this is not the case, the drop can rather be related to a major star formation peak at  $z > 2$  (see below). A decrease of the rest-frame  $(U - V)$  color with increasing redshift up to  $z \approx 3$  was also derived by Kajisawa & Yamada (2005). More detailed comparison with our results is not available at present because in their paper, different morphological types are presented together. The stellar population synthesis model by Bicker et al. (2004) suggests an evolution of  $(U - V)$  by 0.3 magnitudes from  $z = 2$  to  $z = 0$  for Sb galaxies, matching well with our result.

The absolute values of the derived colors are sensitive to photometric calibrations, especially the k-correction, which, in turn, is uncertain. This may cause a vertical shift of  $(U - V)$  datapoints and may be a reason for the generally high value of the derived colors. However, the declining trend in Fig. 4.3 should be independent of these uncertainties.

Recent hydrodynamical simulations of galaxies in  $\Lambda$ CDM cosmology by Robertson et al. (2004) indicate that star formation in disks peaks between redshifts  $z = 2-4$ . Studies of the Fundamental Plane of early-type galaxies at redshifts  $z \leq 1.3$  have also shown that the last epoch of major star formation peaks at  $z = 2-3.5$  (see Holden et al. 2005 and references therein). A jump in star formation beyond redshift  $z = 2$  matches well with the jump in  $(U - V)$  color in Fig. 4.3.

Relying on  $(U - V)$ , we may roughly estimate the disk formation time. According to our photometry, the disks at  $z \approx 2.5$  have  $(U - V) \approx 0.7$  mag. On the basis of simple stellar population chemical evolution models (Worthey 1994; Bressan et al. 1994), these disks have ages 1 – 2 Gyr and have thus formed at  $z = 3.5-7$ .

## 4.4 Color gradients

Fig. 4.4 shows that at redshifts  $z < 2$ , color gradients are small or missing at all. Gradients begin at  $z \approx 2$  and are dominantly positive. A similar rise with redshift of the rest-frame  $(U_{218} - U_{300})$  color gradient was discovered by Moth & Elston (2002); the authors propose that star-formation has been more centrally concentrated at higher redshifts.

Positive color gradients also exist in local disk galaxies (MacArthur et al. 2004) and they may indicate disk formation sequence from inside out. For the Milky Way protogalaxy, such a formation scenario was suggested by van den Bergh (1993). In the case of high-redshift galaxies, direct interpretation of color gradients may be rather complicated. Color gradients

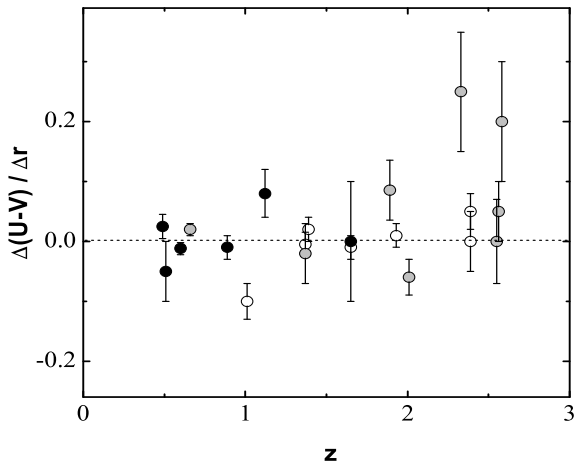


Figure 4.4: Rest frame color gradient  $\Delta(U-V)/\Delta r$  as a function of redshift for the photometric sample galaxies. Designations are the same as in Fig. 4.2.

are determined by radial distribution of initial metallicities, stellar ages, star-formation rate, gas accretion details etc. Dependently on model details, both outside-in and inside-out formation of disks can be simulated (Sommer-Larsen et al. 2003; Robertson et al. 2004). According to the analysis of their disk galaxy formation model, Westera et al. (2002) have found that luminosity from  $U$  to  $V$  mainly indicates star formation, and the effects of age and metallicity are negligible. Thus positive color gradients most possibly refer to intensive star formation in central parts of galaxies at  $z > 2$ .

Smaller color gradients at lower redshifts possibly arise due to smoothing by interactions during disk evolution (Conselice et al. 2005a) and large scale gas motions (Samland & Gerhard 2003).

## 4.5 Masses and mass-to-light ratios

Rotation curve decompositions of the 7 galaxies are given in paper I, Figs 4-9 and paper II, Figs 5-8. With some assumptions applied on the basis of near-by galaxies, we can estimate masses and mass-to-light ratios of the components, according to self-consistent modeling. The small number of galaxies used for modeling does not enable any independent mass evolution

Galaxy name	Hubble type	$z$	$M_B$ (mag)	$M_{vis}$ ( $10^{10} M_\odot$ )	$M_{vis}/L_B$ ( $M_\odot/L_\odot$ )	$\rho(0)_{DM}$ ( $M_\odot/\text{pc}^3$ )
GSS 074-2237	Sc	0.15	-20.0	6.8	4.4	0.009
MDS uem0-043	Sc	0.48	-21.4	7.7	1.4	0.008
HDFS J223247.66-603335.9	Sb(c)	0.58	-21.2	33.9	7.4	0.035
GSS 104-4024	Sbc	0.81	-20.5	10.9	4.3	0.013
GSS 064-4442	Sbc	0.88	-20.4	2.1	0.9	0.022
GSS 094-2210	Sbc	0.90	-21.5	8.6	1.3	0.028
GSS 064-4412	Sc	0.99	-20.6	5.2	1.9	0.012

Table 4.1: Main results of galaxy modeling. Spectroscopic redshift  $z$  is taken from Vogt et al. (1996) and Rigopoulou et al. (2002).  $M_B$  is the absolute  $B$ -magnitude of the galaxies, corrected for absorption inside the Milky Way.  $M_{vis}$  is the total mass of and  $M_{vis}/L_B$  the mass-to-light ratio of visible matter,  $\rho(0)_{DM}$  is the central density of dark matter halos.

analysis. However, the study provides some comparison with other methods and results obtained for local galaxies. Unfortunately, the limited spatial resolution of the observations does not allow saying much about the masses of the bulge components or the DM halos (see Sect. 3.4.5).

The derived masses and mass-to-light ratios of visible matter as well as the central densities for dark matter halos are listed in Tabel 4.1. At a mean redshift  $\langle z \rangle = 0.9$ , our models propose a mean visible mass  $\langle M_{vis} \rangle \approx 7 \cdot 10^{10} M_\odot$  as the higher limit. The average mass-to-light ratio at the same mean redshift is  $\langle M/L_B \rangle = 2.5 M_\odot/L_\odot$ .

Alternatively, stellar masses and mass-to-light ratios can be determined using broadband optical-NIR photometry and chemical evolution models (Drory et al. 2004; Berta et al. 2004). For galaxies at redshifts  $z \approx 0.9$ , Drory et al. (2004) derived  $\langle M/L_B \rangle = 1.3 M_\odot/L_\odot$ , which is somewhat smaller than the present result. For the highest mass galaxies at redshift  $z \approx 0.5$ , they derived  $\langle M/L_B \rangle = 2.6 M_\odot/L_\odot$ , also being smaller than our value 7.4 for the massive galaxy HDFS J223247.66-603335.9. However, within the precision of the models used, these results still agree reasonably; stellar masses of starburst galaxies at  $z \approx 0.5$  have been found to be even up to  $50 \cdot 10^{10} M_\odot$  (Drory et al. 2004, Berta et al. 2004). The derived value at  $\langle z \rangle = 0.9$  can also be compared to the mean stellar  $M/L_B = 2.7 M_\odot/L_\odot$ , calculated by Giraud (1998) for local Sb galaxies; no significant evolution with redshift is detected, which is concordant with the studies of



the TF diagram at intermediate redshifts: Vogt et al. (1996), Ziegler et al. (2003), Conselice et al. (2004), Böhm et al. (2004). An explanation for the changes to be so small can be found from chemical evolution models. Evolution calculations by Bicker et al. (2004, Fig.7) indicate that in the case of Sb galaxies at redshifts  $z \approx 0.5 - 1$ , the k-corrections and evolution corrections nearly compensate each other in the  $B$ -band.

Due to uncertainties in rotation curve determination of high redshift galaxies, caused by lack of resolution and spatial extent, we can determine neither the actual mass of dark matter halos nor the distribution of it. Relying on the central and outer parts of the measured rotation curves, however, we can determine the central densities of the halos,  $\rho(0) = hM/(4\pi a_0^3)$ . Calculated from our models, the central density range of DM components at a mean redshift  $\langle z \rangle = 0.9$  is  $\rho(0) = (0.012 - 0.028) M_{\odot}/\text{pc}^3$ . These values are calculated for maximum disk models and are thus the lower limits. We can compare this result to the mean central density of the DM halos of nine local galaxies  $\rho(0) = (1 - 4) \cdot 10^{-24} \text{g}/\text{cm}^3 = (0.015 - 0.050) M_{\odot}/\text{pc}^3$ , derived by Borriello & Salucci (2001). Although our sample of galaxies is small, there seems to be no significant evolution of DM central density with redshift.

We have also calculated the amount of DM within a half-light radius. For galaxies at redshifts  $\langle z \rangle = 0.9$ , the mean dark matter contribution is  $40 \pm 15$  % of the total mass. Thus, regarding the present sample, the discrepancy between the observed galaxies and CDM models is not as big as indicated in an analysis by Bell et al. (2003).

## 4.6 Uncertainties of the study

While in the case of mass-modeled galaxies the morphological type had already been fixed by several previous studies and their disky nature becomes clear after a brief glance and is also confirmed by the presence of rotation curves, morphological identification of disks at  $z > 1$  often becomes a considerable challenge. Lack of imaging resolution and the faintness of the objects does not allow a straightforward visual classification; furthermore, many objects may be in transition stages (Conselice et al. 2004). Here, the selection of galaxies for the photometric study was initially conducted by a visual inspection of  $H$ -band exposures; all galaxies suspected for being disks of any type were included in the sample. In some cases, the high-resolution STIS  $V$ -band images were also checked. The derived Sérsic index values  $n < 1.5$  encourage to consider the sample to consist of only

disk galaxies.

Some of the galaxies of the present sample have been studied on the basis of NICMOS images by Rodighiero et al. (2001), and classified as E-S0. It is important to note that for classification and accurate photometry, a careful PSF-deconvolution of NICMOS images is necessary. Even in the case of good restoration of NICMOS images, additional observations with other detectors, preferably with higher resolution (e.g. STIS in the present case) still prove beneficial. For example, a visual inspection of the STIS image of the galaxy 419-572 reveals its nature of a late-type, at least Sb galaxy (see Fig. 4.1).

The selection methods of mass-modeled galaxies clearly favor luminous, massive galaxies and no generalizations can be made about the whole population. Galaxies at higher redshifts suffer significantly from the cosmological dimming as  $(1+z)^4$ , thus more luminous galaxies are more likely to be selected for photometry as well. For our photometric sample, Figs 4.2, 4.3 and 4.4 reveal no clear dependence of any of the parameters on the absolute luminosity of the galaxies; this aspect allows us to consider the sample to be sufficiently complete for the conducted analysis.

The selection of the photometric sample on the basis of  $H$ -band imaging (corresponding to rest- $B$  at  $z > 2$ ) might cause a slight bias towards bluer galaxies at higher redshifts. On the other hand, the change of the spectral energy distribution is slow between  $B$  and  $R$  passbands and we consider this possible selection effect not to be a reason for a color jump at  $z \approx 2$  in Fig. 4.3.

For calculating  $k$ -corrections, all galaxies have been assumed to be of Sb morphological type. This approximation causes an additional scatter of absolute magnitudes and colors. Nevertheless, the resulting uncertainties should remain within 0.2 magnitudes even in the worst cases.

As discussed in Sect. 3.4.5, problems with kinematics determinations at high redshifts allow to calculate the actual mass of neither luminous nor dark components. Moreover, knowledge of mass-to-light ratios of visible matter and DM halo masses and mass distribution is limited even in the case of local galaxies. Despite these shortcomings, if a considerable evolution of these parameters would have taken place between  $0 < z < 1$ , it should be detectable with the methods presently used.

Small sample sizes and selectional biases are always critical issues for detailed studies of high-redshift galaxies. The present sample, consisting of 7 galaxies used for mass-decomposition (only 4 galaxies at  $z \approx 0.9$ ) and 22 galaxies used for luminosity distribution and color analysis definitely

can not offer reliable statistics and cautions against jumping into severe conclusions.

Broadening the sample is a matter of the nearest future, however. More mass models can be constructed as soon as the kinematic data from the observations of the FORS Deep Field (Böhm et al. 2004) become available, while a supplementary photometric study of disks can be conducted after more redshifts for distant galaxies in the Hubble Ultra Deep Field (Thompson et al. 2005) are published.

# Chapter 5

## Conclusions

The main results of the present self-consistent mass-distribution modeling and analysis of radial distribution of photometric parameters of distant disk galaxies are presented in the following.

Roughly half of distant disk galaxies show a luminosity decrease clearly steeper than that of a simple exponential disk, indicating disk truncation; such a distribution can well be fitted by Sérsic profiles using index  $n \approx 0.7$ .

Disk sizes have increased remarkably since  $z = 2.6$ ; the sizes scale with redshift as  $r_e(z)/r_e(0) = 1 - 0.26z$ . Within the precision of the current models for hierarchical clustering, this result is in concordance with the predicted evolution.

The overall shape of the luminosity distribution of disk galaxies (the shape parameter  $n$ ) does not change considerably with look-back time.

Blueing of  $(U - V)$  colors by 0.5 magnitudes between  $0.5 < z < 2$  is seen; beyond  $z \approx 2$ , a sudden drop by 0.7 magnitudes is present. On the other hand, beyond  $z \approx 2$ , positive color gradients appear. From these data, a more intense and centrally concentrated star formation may be inferred for disks at these redshifts. Relying on their  $(U - V)$  colors, the disks seen at  $z \approx 2.5$  are 1 – 2 Gyrs old, corresponding to formation at  $z = 3.5 - 7$ .

The mean mass to light ratio for high mass galaxies at  $\langle z \rangle = 0.9$  is  $M/L_B = 2.5 M_\odot/L_\odot$ , which is comparable to the value obtained for local galaxies and thus slightly higher than what is predicted by chemical evolution models.

Within maximum disk assumption, the central density of isothermal dark matter halos of high mass galaxies shows no significant evolution between redshifts  $0 < z < 1$ ; central densities at  $z \approx 0.9$  fall in the range  $\rho(0) = (0.012 - 0.028) M_\odot/\text{pc}^3$

# References

- Abadi, M. G., Navarro, J. F., Steinmetz, M. & Eke, V. R. 2003a, ApJ, 591, 499
- Abadi, M. G., Navarro, J. F., Steinmetz, M. & Eke, V. R. 2003b, ApJ, 597, 21
- Adelberger, K. L. & Steidel, C. C., 2000, ApJ, 544, 218
- Adelberger, K. L., Steidel, C. C., Giavalisco, M. et al., 1998, ApJ, 505, 18
- Allen, P. D., Moustakas, L. A., Dalton, G. et al., 2005, MNRAS, 360, 1244
- Andredakis, Y. C., Peletier, R. F. & Balcells, M., 1995, MNRAS, 275, 874
- Archibald, E. N., Dunlop, J. S., Hughes, D. H. et al., 2001, MNRAS, 323, 417
- Barger, A. J., Cowie, L. L., Trentham, N. et al., 1999, AJ, 117, 102
- Barnes, J. E., 1992, ApJ, 393, 484
- Begeman, K. G., Broeils, A. H., Sanders, R. H., 1991, MNRAS, 249, 523
- Bell, E. F., Baugh, C. M., Cole, S., Frenk, C. S. and Lacey, C. G., 2003, MNRAS, 343, 367
- Bell, E. F. & de Jong, R. S., 2001, ApJ, 550, 212
- Bell, E.F., Wolf, C., Meisenheimer, K., et al., 2004, ApJ 608, 752
- Bendo, G. J. & Barnes, J. E. 2000, MNRAS, 316, 315
- Benson, A. J., Bower, R. G., Frenk, C. S., et al., 2003, ApJ, 599, 38
- Bernardi, M., Sheth, R. K., Annis, J., et al. 2003, AJ, 125, 1882
- Berta, S., Fritz, J., Franceschini, A., Bressan, A. & Lonsdale, C., 2004, A&A, 418, 913
- Bicker, J., Fritze-v. Alvensleben, U., Möller, C.S. & Fricke, K.J., 2004, A&A, 413, 37

- Binney, J. & Merrifield, M., 1998, *Galactic Astronomy*, Princeton Univ. Press
- Binney, J. & Tremaine, S., 1987, *Galactic Dynamics*, Princeton University Press
- Blais-Oullette, S., Amram, P., Carignan, C. & Swaters, R., 2004, *A&A*, 420, 147
- Blakeslee, J. P., Franx, M., Postman, M., et al., 2003, *ApJL*, 596, 143
- Blanton, M.R., Hogg, D.W., Bahcall, N.A., et al., 2003, *ApJ*, 592, 819
- Blumenthal, G. R., Faber, S. M., Primack, J. R. & Rees, M. J., 1984, *Nature*, 311, 517
- Böhm, A., Ziegler, B., Saglia, R.P et al., 2004, *A&A*, 420, 285
- Borriello, A. & Salucci, P., 2001, *MNRAS*, 323, 285
- Bournaud, F., Jog, C. J. & Combes, F., 2005, *A&A*, 437, 69
- Bouwens, R..J. & Silk, J., 2002, *ApJ*, 568, 522
- Bouwens, R. J., Thompson, R. I., Illingworth, G. D. et al., 2004, *ApJ*, 616, L79
- Bouwens, R. J., Illingworth, G. D., Thompson, R. I. & Franx, M., 2005, *ApJ*, 624, L5
- Bressan, A., Chiosi, C., Fagotto, F. 1994, *ApJS*, 94, 63
- Bromm, V. & Larson, V. B., 2004, *ARAA*, 42, 79-118
- Burkert, A., 1995, *ApJ*, 447, L25
- Capaccioli, M., 1989, in *The world of galaxies*, eds. H.G. Corwin, L. Bottinelli, Springer-Verlag, Berlin, p. 208
- Carignan, C., 1985, *ApJ*, 299, 59
- Casertano, S, 1983, *MNRAS*, 203, 735
- Cassata, P., Cimatti, A., Franceschini, A. et al., 2005, *MNRAS*, 357, 903
- Chitre, A. & Jog, C. J., 2002, *A&A*, 388, 407
- Chiosi, C., Carraro, G., 2002, *MNRAS*, 335, 335
- Cimatti, A., Daddi, E., Renzini, A. et al., 2004, *Nature*, 430, 184
- Ciotti, L. & Bertin, G., 1999, *A&A*, 352, 447
- Cole, S., Lacey, C.G., Baugh, C.M. & Frenk, C.S. 2000, *MNRAS*, 319, 168
- Coleman, G.D., Wu, C.-C. & Weedman, D.W. 1980, *ApJS*, 43, 393
- Colless, M., Dalton, G., Maddox, S., et al., 2001, *MNRAS*, 328, 1039
- Connolly, A. J., Szalay, A. S., Dickinson M. et al., 1997, *ApJL*, 486, 11

- Conselice, C. J., Bundy, K., Ellis, R. S., Brinchmann, J. and Vogt, N., 2004, in *Dark Matter in Galaxies*, IAU Symp 220, 21-25 July 2003, ed.-s S. D. Ryder, D. J. Pisano, M. A. Walker and K. C. Freeman (ASP)
- Conselice, C.J., Bundy, K., Ellis, R.S., et al. 2005a, *ApJ*, 628, 160
- Conselice, C.J., Grogan, N.A., Jogee, S., et al. 2004, *ApJ*, 600, L139
- Conselice, C. J., Vreeswijk, P.M., Fruchter, A.S., et al., 2005b, *ApJ*, 633, 29
- Corbin, M. R., Vacca, W. D., O'Neil, E. et al., 2000, *AJ*, 119, 1062
- Cowie, L., Songaila, A. & Barger, A. J., 1999, *AJ*, 117, 2656
- de Bernadis, P., Ade, P. A. R., Bock, J. J. et al. 2002, *ApJ*, 564, 559
- de Blok, W. J. G., McGaugh, S. S. & Rubin, V. C., 2001, *AJ*, 122, 2396
- de Grijs, R., Kregel, M., Wesson, K. H., 2001, *MNRAS*, 324, 1074
- de Lapparent, V., Galaz, G., Bardelli, S. & Arnouts, S., 2003, *A&A*, 404, 831
- Dickinson, M. & Sosey, M., 2002, *NICMOS Photometric Calibration*, HST Calibration Workshop, Space Telescope Science Institute, 2002, S. Arribas, A. Koekemoer and B. Whitmore, eds.
- Djorgovski, S. & Davis, M., 1987, *ApJ*, 313, 59
- Dolphin, A., 2000, *PASP* 112, 1397
- Doroshkevich, A., Tucker, D. L., Allam, S. & Way, M. J., 2004, *A&A*, 418, 7
- Dressler, A. 1980, *ApJ*, 236, 351
- Dressler, A, Lynden-Bell, D., Burstein, D., et al., 1987, *ApJ*, 313, 42
- Drory, N., Bender, R., Feulner, G., et al. 2004, *ApJ*, 608, 742
- Dutton, A. A., Courteau, S., de Jong, R. & Carignan. 2005, *ApJ*, 619, 218
- Eggen, O. J., Lynden-Bell, D. & Sandage, A. R., 1962, *ApJ*, 136, 748
- Einasto, J. 1969, *Astrofizika*, 5, 137
- Einasto, J. & Haud, U. 1989, *A&A*, 223, 89
- Einasto, J., Kaasik, A. & Saar, E., 1974, *Nature*, 250, 309
- Erb, D.K., Shapley, A.E., Steidel, C.C., et al. 2003, *ApJ*, 591, 101
- Erwin, P., Beckman, J. E., Pohlen, M., 2005, *ApJ*, 626, L81
- Faber, S. M. & Jackson, R. E., 1976, *ApJ*, 204, 668
- Faber, S. M. & Gallagher, J. S., 1979, *ARAA*, 17, 135

- Fall, S. M. & Efstathiou, G., 1980, MNRAS, 193, 189
- Ferguson, H.C., Dickinson, M., Giavalisco, M., et al. 2004, ApJ, 600, L107
- Forbes, D. A., Elson, R. A. W., Phillips, A. C., Koo, D. C. & Illingworth, G. D., 1994, ApJ, 437, L17
- Franceschini, A., Silva, L., Fasano, G. et al., 1998, ApJ, 506, 600
- Freedman, W. L. & Turner, M. S., 2003, Rev. Mod. Phys. 75, 1433
- Freeman, K. C. 1970, ApJ, 160, 811
- Fukushige, T. & Makino, J., 1997, ApJ, 477, L9
- Gabasch, A., Bender, R., Seitz, S. et al., 2004, A&A, 421, 41
- Gallego, J., Zamorano, J., Aragon-Salamanca, A. & Rego, M., 1995, ApJ, 455, L1
- Giraud, E., 1998, AJ, 116, 1125
- Glazebrook, K., Ellis, R., Santiago, B. & Griffiths, R., 1995, MNRAS, 275, L19
- Governato, F., Mayer, L., Wadsley, J. et al., 2004, ApJ, 607, 688
- Gramann, M., 1988, MNRAS, 234, 569
- Griffiths, R. E., Ratnatunga, K. U., Neuschaefer, L. W. et al., 1994, ApJ, 437, 67
- Heavens, A., Panter, B., Jimenez, R. & Dunlop, J., 2004, Nature, 428, 625
- Hernández-Toledo, H. M. & Puerari, I, 2001, A&A, 379, 54
- Hibbard, J. E. & Mihos, J. C., 1995, AJ, 110, 140
- Holden, B. P., et al. 2005, ApJ, 607, L83
- Holtzman, J., A., Burrows, C. J., Casertano, S., et al., 1995, PASP, 107, 1065
- HST Data Handbook for NICMOS, Version 6.0, Space Telescope Science Institute, July 2004
- Im, M., Faber, S. M., Gebhardt, K., et al., 2001, AJ, 122, 750
- Iverson, R. J., Smail, I., Bentz., M. et al., 2005, MNRAS, 362, 535
- Jarrett, T. H., Chester, T., Cutri, R., et al. 2000, AJ, 119, 2498
- Jing, Y. P. & Suto, Y., 2000, ApJ, 529, L65
- Junqueira, S., Mello, D.F. & Infante, L., 1998, AAS, 129, 69
- Kashlinsky, A., 2005, ApJ 633, L5
- Katz, N. & Gunn, J. E. 1991, ApJ, 377, 365



- Kauffmann, G. & Charlot, S., 1998, MNRAS, 297, L23
- Kauffmann, G., Colberg, J. M., Diaferio, A., & White, S. D. M. 1999, MNRAS, 303, 188
- Kelson, D. D., van Dokkum, P. G., Franx, M., Illingworth, G. D. and Fabricant, D., 1997, ApJ, 478, 13.
- Kennicutt, R.C., 1989, ApJ, 344, 685
- Kodama, T. & Arimoto, N. 1997, A&A, 320, 41
- Kogut A, Spergel D.N., Barnes C., Bennett C.L., Halpern M. et al. 2003. ApJS 148, 161
- Koo, D. C., Vogt, N. P., Phillips, A. C. et al., 1996, ApJ, 469, 535
- Kormendy, J. & Kennicutt, R. C., Jr. 2004, ARAA, 42, 603
- Kregel, M. & van den Kruit, P. C., 2005, MNRAS, 358, 481
- Larson, R., 1975, MNRAS, 173, 671
- Lilly S.J., Tresse L., Hammer F., Crampton D., Le Fèvre O., 1995, ApJ, 455, 108
- Lilly, S., Le Fèvre, O., Hammer, F. & Crampton, D., 1996, ApJL, 460, 1
- Lin, H., Yee, H.K.C., Carlberg, R.G. et al., 1999, ApJ, 518, 533
- Lucas, R.A., Baum, S.A., Brown, T.M., et al., 2003, AJ, 125, 398
- Lynden-Bell, D. 1967, MNRAS, 136, 101
- MacArthur, L.A., Courteau, S., Bell, E., Holtzman, J.A. 2004, ApJS, 152, 175
- Mazure, A. & Capelato, H. V. 2002, A&A, 383, 384
- Menci, N., Cavaliere, A., Fontana, A., et al. 2003, astro-ph/0311496
- Melott, A. L., Einasto, J., Saar, E. et al., 1983, Phys. Rev. Lett., 51, 935
- Miley, G. K., Overzier, R. A., Zlatan, I. et al., 2004, Nature, 427, 47
- Milgrom, M., 1983, ApJ, 270, 365
- Miyamoto, M. & Nagai, R. 1975, PASJ, 27, 533
- Mo, H. J., Mao, S., & White, S. D. M., 1998, MNRAS, 295, 319
- Moore, B., Quinn, T., Governato, F., Stadel, J. & Lake, G., 1999, MNRAS, 310, 1147
- Moriondo, G., Giovanardi, C., Hunt, L. K., 1998, A&AS, 130, 81
- Naab, T. & Burkert, A. 2003, ApJ, 597, 893
- Navarro, J. F. & Benz, W. 1991, ApJ, 380, 320
- Navarro, J. F., Frenk, C. S. and White, S. D. M., 1996, ApJ, 462, 563

- Navarro, J.F., Hayashi, E., Power, C. et al., 2004, MNRAS, 349, 1039
- Navarro, J. F. & Steinmetz, M., 2000, ApJ, 538, 477
- Navarro, J. F. & White, S. D. M., 1993, MNRAS, 265, 271
- Navarro, J. F. & White, S. D. M., 1994, MNRAS, 267, 401
- Near Infrared Camera and Multi-Object Spectrometer Instrument Handbook for Cycle 14, Space Telescope Science Institute, 2004
- Norberg P., Cole S., Baugh C.M. et al., 2002, MNRAS, 336, 907
- Oke, J. B. & Sandage, A., 1968, ApJ, 154, 210
- Ouchi, M., Shimasaku, K., Okamura, S. et al., 2004, ApJ, 611, 685
- Palunas, P. & Williams, T. B., 2000, AJ, 120, 2884
- Papovich, C., Dickinson, M., Ferguson, H. C., 2001, ApJ, 559, 620
- Papovich, C., Giavalisco, M., Dickinson, M., Conselice, C. J. and Ferguson, H. C., 2003, ApJ, 598, 827
- Partridge, R. B. & Peebles, P. J., 1967, ApJ, 147, 868
- Pérez, I., 2004, A&A, 427, 17
- Persic, M. & Salucci, P., 1995, ApJS, 99, 501
- Pettini, M., Shapeley, A. E., Steidel, C. C. et al., 2001, ApJ, 554, 981
- Pohlen, M., Dettmar, R-J, Lütticke, R. and Aronica, G., 2002, A&A, 392, 807
- Prugniel, P., Simien, F., 1997, A&A, 321, 111
- Ravindranath, S., Ferguson, H. C., Conselice, C., Giavalisco, M. et al., 2004, ApJ, 604, L9
- Reshetnikov, V.P., Hagen-Thorn, V.A. & Yakovleva, V.A, 1993, AAS, 99, 257
- Reuland, M., Röttgering, H. & van Breugel, W., 2003, New Astron. Rev, 47, 303
- Robertson, B., Yoshida, N., Springel, V. & Hernquist, L., 2004, ApJ, 606, 32
- Rodighiero, G., Franceschini, A., & Fasano, G., 2001, MNRAS 324, 491
- Samland, M. & Gerhard, O.E. 2003, A&A, 399, 961
- Sanders, R. H., 1990, A&A Rev., 2, 1
- Sasaki, T., 1987, PASJ, 39, 849
- Sawicki, M. & Yee, H. K. C., 1998, AJ, 115, 1329
- Schlegel, D.J., Finkbeier, D.P. & Davis, M. 1998, ApJ, 500, 525

- Schneider R., Ferrara A., Salvaterra R., Omukai K., Bromm V., 2003, Nature, 422, 869
- Schweizer, F. 1982, ApJ, 252, 455
- Sérsic, J. L. 1968, Atlas de Galaxies Australes, Observatorio Astronomico, Cordoba, Argentina
- Shen, S., Mo, H. J., White, S. D. M., Blanton, M. R. et al., 2003, MNRAS, 343, 978
- Simon, J. D., Bolatto, A. D., Leroy, A. & Blitz, L., 2003, ApJ, 596, 957
- Sofue, Y. & Rubin, V., 2001, ARAA, 39, 137
- Sommer-Larsen, J., Gtz, M. and Portinari, L., 2003, ApJ, 596, 47
- Spergel, D. N., Verde, L., Peiris, H. V. et al., 2003, ApJS, 148, 175
- Stanford, S.A. & Bushouse, H.A., 1991, ApJ, 371, 92
- Steidel, C. C. & Hamilton, D. D., 1992, AJ, 104, 941
- Steinmetz, M. & Müller, E. 1994, A&A, 281, L97
- Steidel, C.C., Adelberger, K.L., Giavalisco, M., Dickinson, M. & Pettini, M., 1999, ApJ, 519, 1
- Steidel, C. C., Adelberger, K. L., Shupeley, A., Pettini, M., 2003, ApJ, 592, 728
- Stevens, J.A., Ivison, R. J., Dunlop, J. S. et al., 2003, Nature, 425, 264
- Swaters, R. A., Madore, B. F., & Trehella, M. 2000, ApJ, 531, L107
- Takamiya, T. & Sofue, Y., 2000, ApJ, 534, 670
- Tanaka, M., Kodama, T., Arimoto, N., et al., 2005, MNRAS 362, 268
- Tenjes, P., Haud, U., Einasto, J., 1994, A&A, 286, 753
- Tenjes, P., Haud, U., Einasto, J., 1998, A&A, 335, 449
- Thompson, R. I., Storrie-Lombardi L. J., Weymann, R. J. et al., 1999, AJ, 117, 17
- Thomson R. C., Wright A. E., 1990, MNRAS, 247, 122
- Toomre, A. 1977, in The Evolution of Galaxies and Stellar Populations, eds. B.M. Tinsley, & R.B. Larson (New Haven: Yale Univ. Obs.), 401
- Treu, T., Stiavelli, M., Casertano, S., Moller, P. and Bertin, G., 2000, MNRAS, 333, 510
- Trujillo, I., Rudnick, G., Rix, H.-W., Labbé I., et al., 2004, ApJ, 604, 521
- Trujillo, I., Schreiber, N.M.F., Rudnick, G., et al. 2005, ApJ submitted (astro-ph/0504225)

- Trujillo, I. & Pohlen, M., 2005, ApJ, 630, L17
- Tully, R. B. & Fisher, J. R., 1977, A&A, 54, 661
- Turnbull, A. J., Bridges, T. J. & Carter, D., 1999, MNRAS, 307, 967
- van den Bergh, S., 1993, ApJ, 411, 178
- van den Bergh, S., Cohen, J. G. & Crabbe, C., 2001, AJ, 122, 611
- van den Bosch, F., 2001, MNRAS, 327, 1334
- van den Bosch, F. C., Robertson, B. E., Dalcanton, J. J., & de Blok, W. J. G. 2000, AJ, 119, 1579
- van den Kruit, P. C., Jiménez-Vicente, J., Kregel, M. & Freeman, K. C., 2001, A&A, 379, 374
- van Dokkum, P. G. & Franx, M. 1996, MNRAS, 281, 985
- van Dokkum, P. G., Franx, M., Fabricant, D., Illingworth, G. D., & Kelson, D. D. 2000, ApJ, 541, 95
- van Dokkum, P. G., Franx, M., Kelson, D. D. and Illingworth, G. D., 2001, ApJ, 553, L39
- Visvanathan, N. & Sandage, A., 1977, ApJ, 216, 214
- Vogt, N. P., Forbes, D. A., Phillips, A. C., et al. 1996, ApJ, 465, L15
- Weiner, B. J., Phillips, A. C., Faber, S. M. et al., 2005, ApJ, 620, 595
- Westera, P., Samland, M., Buser, R. & Gerhard, O. E., 2002, A&A, 389, 761
- White, S. D. M. & Rees, M. J. 1978, MNRAS, 183, 341
- Whitmore, B., Heyer, I., Casertano, S., 1999, PASP, 111, 1559
- Wilkinson, A., Prieur, J.-L., Lemoine, R. et al., 2000, MNRAS, 319, 977
- Williams, R.E., Baum, S., Bergeron, L.E., et al., 2000, AJ, 120, 2735
- Windhorst, R. A., Taylor, V. A., Jansen, R. A. et al., 2002, ApJS, 143, 113
- Wolf, C., Meisenheimer, K., Rix, H.-W. et al., 2003, A&A, 401, 73
- Worthey, G., 1994, ApJS, 95, 107
- Wuyts, S., van Dokkum, P. G., Kelson, D. D., Franx, M. and Illingworth, G. D., 2004, ApJ, 605, 677.
- Yahata, N., Lanzetta, K. M., Chen, H.-W. et al., 2000, ApJ, 538, 493
- York, D. G. et al., 2000, AJ, 120, 1579
- Zhang, B. & Wyse, R., 2000, MNRAS, 313, 310
- Ziegler, B. L., Böhm, A., Jäger, K., Heidt, J. and Möllenhoff, C., 2003, ApJ, 598, 87

# Kokkuvõte

## Kaugele ketasgalaktikate struktuur

Viimase paarikümne aasta jooksul toimunud astronoomilise vaatlustehnika hüppeline areng on tänaseks loonud olukorra, kus galaktikate ja Universumi üldisema struktuuri kujunemist saab jälgida vahetute vaatluste abil. Käesolevas töös keskendutakse ketasgalaktikate heleduse-, värvuse- ja massijaotuse evolutsiooni uurimisele, kasutades Hubble kosmoseteleskoobi arhiivivaatlusi optilises ja infrapunases spektriosas ning Keck'i ja VLT teleskoopidega mõõdetud galaktikate pöörlemiskõveraid.

Massijaotuse konstrueerimiseks kõrvutatakse suhtelistel punanihetel  $z < 1$  asuva seitsme galaktika kohta saadud heledusjaotusi ja pöörlemiskõveraid. Mudel-heledusjaotuste ja -pöörlemiskiiruste arvutamiseks lähtutakse samast ruumtihedusejaotusest (valem 3.6); niiviisi luuakse kooskõlaline massijaotusmudel. Sobitades mudeljaotusi vaadeldud kõveratega, määratakse nähtavate komponentide raadiused, nähtava aine tihedusjaotuse profiili kõverus ja mass-heleduse suhted ning tumeda aine keskne tihedus. Masside määramisel kasutatakse nn. maksimaalse ketta lähendust. Ühelgi juhul ei ulatu pöörlemiskiiruste vaatlused kaugemale kui 20 kiloparsekit galaktika keskmest, sestap lähtutakse modelleerimisel eeldusest, et pöörlemiskiirused jäävad suurematel kaugustel ligikaudu muutumatuks, nii nagu on kindlaks tehtud lähemate galaktikate puhul.

Galaktikate pindheleduse analüüsi saab läbi viia ka märkimisvääraselt suurematel punanihetel. Punanihete vahemikus  $0.5 < z < 2.6$  asuva 22 galaktika kohta koostatakse heledus- ja värvusjaotuste kõverad. Selleks kasutatakse hea nurklahutusega ja suure vaatlussügavusega infrapuna-seid ja optilisi ülevõtteid, mis on tehtud NICMOS ja STIS kaameratega HDF-Lõuna programmi raames. Kasutadaolevad vaatlused  $V$ -,  $J$ - ja  $H$ -filtriribas võimaldavad kaasaliikuva taustsüsteemi  $B$ -heleduse ja  $(U - V)$ -värvuse jaotuse tuletamist. Vastavad  $k$ -korrektsioonid leitakse keemise evolutsiooni mudelite alusel koostatud sünteetiliste spektrite põhjal. Saadud

heledusprofiilid lähendatakse Sérsicu mudeljaotusega (valem 3.3); selleks tuletatakse väikeste kõverusparameetri  $n$  väärtustele vastava normeerimis-konstandi lähendusvalem (3.5).

Tulemused osutavad, et ligikaudu poolel uuritud ketasgalaktikatest kahaneb heledusjaotus kiiremini kui lihtne eksponentsiaalne mudel. Sellist profiili saab hästi lähendada nii ruumtiheduse (3.6) põhjal leitud mudeljaotusega kui ka Sérsicu mudeljaotusega, kasutades kujuparameetri väärtusi  $0.5 < n < 1$ . Käesoleva valimi punanihetevahemikus ei esine märkimisväärset heledusjaotuse muutust.

Punanihke suurenedes kahanevad ketaste mõõtmed oluliselt, vastavalt lineaarsele lähendusele  $r_e(z)/r_e(0) = 1 - 0.26z$ . Antud tulemus on üsna heas koosõlas mudelite põhjal ennustatava sõltuvusega, arvestades hetkel olemasolevate aine hierarhilise kuhjumise mudelite täpsust.

$(U - V)$  värvusindeksid näitavad sininemist koos punanihke suurenemisega vahemikus  $0.5 < z < 2$ ; punanihetel  $z > 2$  ilmneb värvusindeksi kukkumine ligikaudu 0.7 tähesuuruse võrra. Alates punanihkest  $z \approx 2$  ilmuvad positiivsed värvigradiendid. Nendest tulemustest võib järeldada, et punanihetel  $z \approx 2$  ja varem on täheteked olnud intensiivsem ning keskele koondunud; sarnast tendentsi on märkinud ka Moth ja Elston (2002). Keemilise evolutsiooni mudelitest lähtuvalt saab värvusindeksite põhjal hinnata galaktikate ligikaudset vanust. Punanihetel  $z \approx 2.5$  asuvate galaktikate korral saadakse vanuseks 1 – 2 miljardit aastat, mis vastab tekkepunanihkele  $z = 3.5 - 7$ .

Punanihkel  $\langle z \rangle = 0.9$  leitakse suure massiga galaktikate keskmiseks mass-heleduse suhteks  $M/L_B = 2.5M_\odot/L_\odot$ , mis on võrreldav lähedaste galaktikate vastavate väärtustega ning mõnevõrra suurem kui ennustavad keemilise evolutsiooni mudelid. Uuritud vahemikus  $0 < z < 1$  ei ilmne tumeda aine halode keskse tiheduse märgtavat muutust; punanihetel  $z \approx 0.9$  jääb keskne tihedus vahemikku  $\rho(0) = (0.012 - 0.028) M_\odot/\text{pc}^3$ .

# Acknowledgements

I feel most indebted to my supervisor Dr. Peeter Tenjes, who has initiated these studies and has consistently helped me to overcome any obstacle on the bumpy road of becoming an astrophysicist in the given space-time.

I wish to thank Drs Paolo Salucci, Asmus Böhm and Mirt Gramann for useful comments and discussions and Dr. Urmas Haud for making available his software for galactic model calculations. I thank Dr. Nicole Vogt for enabling the usage of his kinematics data.

Carrying out this study has become possible due to the existence of the STScI archive and I express my gratitude to all the people involved.

I acknowledge the financial support from the Estonian Science Foundation (research grants 4702 and 6106).

# Publications



# CURRICULUM VITAE

## ANTTI TAMM

Date and place of birth: June 14, 1977, Tartu  
Citizenship: Estonian  
Marital status: Bachelor  
Address: Tartu Observatory, Tõravere, 61602, Estonia  
Phone: (+372) 741 0450  
*e-mail*: atamm@ut.ee  
Current position Tartu Observatory, research associate

### Education

2001– University of Tartu, Ph.D. student  
1999–2001 University of Tartu, graduate student, M.Sc. 2001  
(astrophysics)  
1995–1999 University of Tartu, student, B.Sc. 1999 (physics)  
1984–1995 Tartu Miina Härma High School (silver medal)

### Work experience

2005– Tartu Observatory, research associate

### Scientific work

Main fields of research: Formation, structure and evolution of galaxies; dark matter distribution in the Universe; dark matter halos around galaxies

Number of publications:4

## **Professional self-improvement**

Summerschool "*Cosmology and the High-Redshift Universe*", August 5–15, 2002, Abisko, Sweden

Winterschool "*Physics of Galaxy Formation*", December 16–30, 2003, Harish-Chandra Research Institute, Allahabad, India.

Winterschool "*On the origin of galaxies*", 29.12.2003 – 8.01.2004, The Institute for Advanced Studies, The Hebrew University of Jerusalem, Israel.

# ELUKÄIK

## ANTTI TAMM

Sünniaeg ja koht: 14. juuni 1977, Tartu  
Kodakondsus: Eesti  
Perekonnaseis: Vallaline  
Aadress: Tartu Observatoorium, Tõravere, 61602, Eesti  
Telefon: (+372) 741 0450  
*e-mail*: atamm@ut.ee  
Töökoht: Tartu Observatoorium, teadur

### Hariduskäik

2001– TÜ doktorant  
1999–2001 TÜ magistrant, M.Sc. 2001 (astrofüüsika)  
1995–1999 TÜ üliõpilane, B.Sc. 1999 (füüsika)  
1984–1995 Tartu Miina Härma Gümnaasium (hõbemedal)

### Teenistuskäik

2005– Tartu Observatoorium, teadur

### Teadustegevus

Peamised töösuunad: Galaktikate teke, evolutsioon ja struktuur; tumeda aine jaotus Universumis; tumeda aine halod galaktikate ümber

Publikatsioone: 4

## **Erialane enesetäiendus**

Suvekool "*Cosmology and the High-Redshift Universe*", 5.–15. august 2002, Abisco, Rootsi

Talvekool "*Physics of Galaxy Formation*", 16.–30. detsember, 2003, Harish-Chandra Research Institute, Allahabad, India

Talvekool "*On the origin of galaxies*", 29.12.2003–8.01.2004, The Institute for Advanced Studies, The Hebrew University of Jerusalem, Iisrael